

Dr Nakao Summer Research Notebook

Dylan Jacobs

May 2024

1 Week 2: 5/27/2024

1.1 Lax-Wendroff Modified Equation

We start with the linear advection equation

$$u_t + u_x = 0$$

with an advection speed of $a = 1$.

If we analyze the Lax-Wendroff numerical approximation of this partial differential equation (PDE) is defined as follows:

$$u_j^{n+1} = u_j^n - \frac{a\Delta t}{2\Delta x}(u_{j+1}^n - u_{j-1}^n) + \frac{a^2\Delta t^2}{2\Delta x^2}(u_{j+1}^n - 2u_j^n + u_{j-1}^n)$$

We assume that there is a function $v(x, t)$ that satisfies the Lax-Wendroff numerical approximation of this PDE. Then, the Lax-Wendroff Equation becomes

$$v(x_j, t_{n+1}) = v(x_j, t_n) - \frac{a\Delta t}{2\Delta x}(v(x_{j+1}, t_n) - v(x_j, t_n)) + \frac{a^2\Delta t^2}{2\Delta x^2}(v(x_{j+1}, t_n) - 2v(x_j, t_n) + v(x_{j-1}, t_n))$$

Reorganizing terms yields

$$\frac{v_j^{n+1} - v_j^n}{\Delta t} + \frac{v_{j+1}^n - v_{j-1}^n}{2\Delta x} = \frac{\Delta t(v_{j+1}^n - 2v_j^n + v_{j-1}^n)}{2\Delta x^2}$$

We can use Taylor Series Expansions around both v_j and v^n to get

$$\begin{aligned} & \frac{1}{\Delta t}[v_j^n + \Delta t(v_j^n)_t + \frac{1}{2}(\Delta t^2(v_j^n)_{tt}) + \frac{1}{6}(\Delta t^3(v_j^n)_{ttt}) + \dots - v_j^n] \\ & + \frac{1}{2\Delta x}[(v_j^n + \Delta x(v_j^n)_x + \frac{1}{2}(\Delta x^2(v_j^n)_{xx}) + \frac{1}{6}(\Delta x^3(v_j^n)_{xxx}) + \dots \\ & \quad - (v_j^n - \Delta x(v_j^n)_x + \frac{1}{2}(\Delta x^2(v_j^n)_{xx}) - \frac{1}{6}(\Delta x^3(v_j^n)_{xxx}) + \dots)] \\ & = \frac{\Delta t}{2\Delta x^2}[(v_j^n + \Delta x(v_j^n)_x + \frac{1}{2}(\Delta x^2(v_j^n)_{xx}) + \frac{1}{6}(\Delta x^3(v_j^n)_{xxx}) + \dots \\ & \quad + (v_j^n - \Delta x(v_j^n)_x + \frac{1}{2}(\Delta x^2(v_j^n)_{xx}) - \frac{1}{6}(\Delta x^3(v_j^n)_{xxx}) + \dots \\ & \quad \quad \quad - 2v_j^n] \end{aligned}$$

We see that terms cancel, yielding

$$v_t + \frac{1}{2}\Delta t v_{tt} + \frac{1}{6}\Delta t^2 v_{ttt} + \mathcal{O}(\Delta t^3) + v_x + \frac{1}{6}\Delta x^2 v_{xxx} + \mathcal{O}(\Delta x^4) = \frac{1}{2}\Delta t v_{xx} + \Delta t \mathcal{O}(\Delta x^2)$$

We know that $v_{tt} = a^2 v_{xx}$ and $v_{ttt} = -a^3 v_{xxx}$, so we can further simplify

$$v_t + v_x = \frac{1}{6}(\Delta t^2 - \Delta x^2) v_{xxx} + \mathcal{O}(\Delta x^3) + \mathcal{O}(\Delta t^3)$$

We can see that v models a dispersive PDE, as indicated by the v_{xxx} term.

1.2 Upwind Scheme in MATLAB

Consider the linear advection equation

$$u_t + u_x = 0, \quad x \in [0, 1]$$

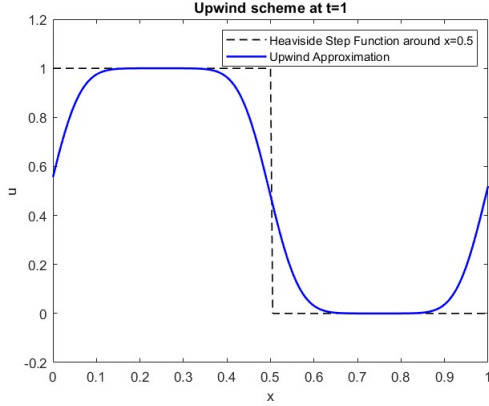
with the initial condition

$$u_0(x) = \begin{cases} 1, & x \leq 0.5 \\ 0, & x > 0.5 \end{cases}$$

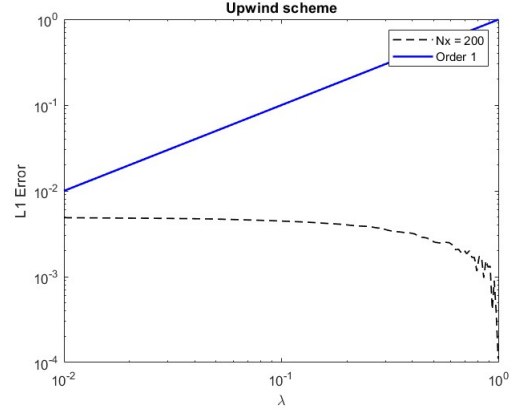
We can approximate this PDE at the final time $T_f = 1$ using an upwind scheme, given by

$$u_j^{n+1} = u_j^n - \frac{\Delta t}{\Delta x} (u_j^n - u_{j-1}^n)$$

Figure 1a shows the approximate solution at $t = 1$. There is some smearing due to the first-order nature of the upwind forward-Euler forward-difference method. This method's spatial accuracy is shown in Table 1 and the temporal accuracy is shown in Figure 1b (it does not converge to first-order accuracy because the time-step size is too small, as required by the stability constraint. However, it is clear that the spatial accuracy converges to $\mathcal{O}(\Delta x)$ as Δx halves. The MATLAB code is located in the Week 2 Appendix section.



(a) Solution curve for upwind scheme with mesh size $N_x = 200$ approximating the Heaviside Step function around $x = 0.5$



(b) Temporal error plot for upwind scheme with mesh size $N_x = 200$ approximating the linear advection equation with $u_0(x) = \sin 2\pi x$.

Figure 1: Upwind Scheme Plots

N_x	L^1 Error	L^1 Order	L^2 Error	L^2 Order
20	0.2869	-	0.3116	-
40	0.1627	0.818	0.1786	0.8029
80	0.0871	0.9016	0.096	0.8951
160	0.0451	0.9504	0.0498	0.946
320	0.0229	0.976	0.0254	0.9728
640	0.0115	0.9887	0.0128	0.9865

Table 1: Upwind spatial convergence table (converging to $\mathcal{O}(\Delta x)$) approximating the linear advection equation with $u_0(x) = \sin 2\pi x$.

1.3 Lax-Wendroff Method in MATLAB

Consider now the linear advection equation

$$u_t + u_x = 0, \quad x \in [0, 1]$$

with the identical initial condition

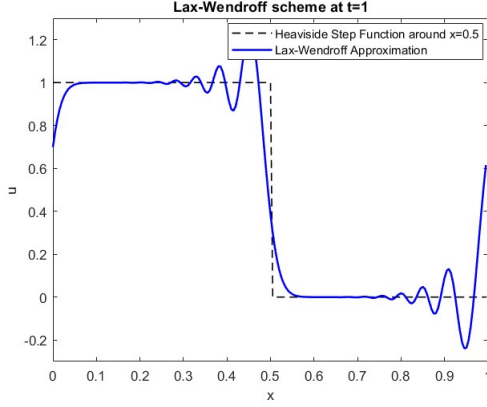
$$u_0(x) = \begin{cases} 1, & x \leq 0.5 \\ 0, & x > 0.5 \end{cases}$$

We can better approximate this PDE at the final time $T_f = 1$ using the Lax-Wendroff method, given by

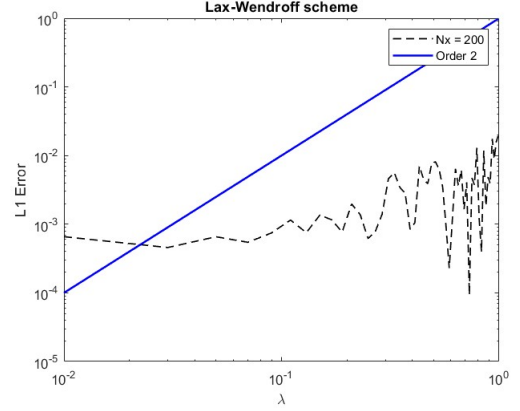
$$u_j^{n+1} = u_j^n - \frac{a\Delta t}{2\Delta x}(u_{j+1}^n - u_{j-1}^n) + \frac{a^2\Delta t^2}{2\Delta x^2}(u_{j+1}^n - 2u_j^n + u_{j-1}^n)$$

where the advection speed $a = 1$.

Figure 2a shows the approximate solution at $t = 1$. There is some smearing due to the first-order nature of the upwind forward-Euler forward-difference method. This method's spatial accuracy is shown in Table 2 and the temporal accuracy is shown in Figure 2b (it does not converge to second-order accuracy because the time-step size is too small, as required by the stability constraint). However, it is clear that the spatial accuracy converges to $\mathcal{O}(\Delta x^2)$ as Δx halves. The MATLAB code is located in the Week 2 Appendix section.



(a) Solution curve for Lax-Wendroff Method with mesh size $N_x = 200$ approximating the Heaviside Step function around $x = 0.5$



(b) Temporal error plot for Lax-Wendroff Method with mesh size $N_x = 200$ approximating the linear advection equation with $u_0(x) = \sin(2\pi x)$ around $x = 0.5$

Figure 2: Lax-Wendroff Method Plots

N_x	L^1 Error	L^1 Order	L^2 Error	L^2 Order
20	0.0491	-	0.0543	-
40	0.0123	1.9928	0.0137	1.9883
80	0.0031	1.9989	0.0034	1.9978
160	0.0008	1.9998	0.0009	1.9995
320	0.0002	2.0000	0.0002	1.9999
640	0.0000	2.0000	0.0001	2.0000

Table 2: Lax-Wendroff spatial convergence table (converging to $\mathcal{O}(\Delta x^2)$) approximating the linear advection equation with $u_0(x) = \sin(2\pi x)$ around $x = 0.5$

2 Week 3: 6/3/2024

2.1 Lax-Friedrichs Method

2.1.1 Order of Accuracy

We now consider the Inviscid Burgers' Equation

$$u_t + \left(\frac{1}{2}u^2\right)_x = 0$$

This can be written in the non-conservative form

$$u_t + uu_x = 0$$

This form is equivalent to the advection PDE, where the advection speed equals the value of the advected quantity (u).

We can approximate this PDE using the Lax-Friedrichs Method

$$\bar{u}_j^{n+1} = \bar{u}_j^n - \frac{\Delta t}{\Delta x} (\hat{f}_{j+\frac{1}{2}} - \hat{f}_{j-\frac{1}{2}})$$

where $\hat{f}(u^-, u^+)$ represents the numerical flux function, approximating the true flux function $f(u)$ at u_j . \hat{f} can be approximated by the first-order method

$$\hat{f}_{j+\frac{1}{2}} = \hat{f}(\bar{u}_j, \bar{u}_{j+1}) = \frac{1}{2}(f(\bar{u}_j) + f(\bar{u}_{j+1})) + \frac{\alpha}{2}(\bar{u}_j - \bar{u}_{j+1})$$

$$\hat{f}_{j-\frac{1}{2}} = \hat{f}(\bar{u}_j, \bar{u}_{j-1}) = \frac{1}{2}(f(\bar{u}_j) + f(\bar{u}_{j-1})) + \frac{\alpha}{2}(\bar{u}_{j-1} - \bar{u}_j)$$

We can test the error and order of accuracy of the Lax-Friedrichs approximation of Burgers' Inviscid Equation with smooth initial condition $u_0(x) = \sin x$ along the interval $x \in [-\pi, \pi]$ at final time $T_f = 0.5$. We find that the Lax-Friedrichs Method converges to first-order spatial accuracy ($\mathcal{O}(\Delta x)$) in both the L^1 and L^2 norms, as shown in Table 3.

N_x	L^1 Error	L^1 Order	L^2 Error	L^2 Order
10	1.32	-	6.39E-1	-
20	6.86E-1	9.49E-1	3.42E-1	9.00E-1
40	3.34E-1	1.04	1.71E-1	1.00
80	1.63E-1	1.03	8.60E-2	9.88E-1

Table 3: Lax-Friedrichs spatial convergence table (converging to $\mathcal{O}(\Delta x)$) approximating Burgers' Equation with $u_0(x) = \sin x$ at $T_f = 0.5$.

2.1.2 Riemann Problem 1

Knowing the Lax-Friedrichs Method converges to first-order spatial accuracy, we can test this algorithm on discontinuous Riemann data. We first consider Burgers' Equation with initial data

$$u_0(x) = \begin{cases} 1, & x \leq 0 \\ -0.5, & x > 0 \end{cases} \quad (1)$$

We can approximate this PDE along the interval $x \in [-\pi, \pi]$ using the spatial mesh size $N_x = 160$, with the CFL condition $\frac{\Delta t}{\Delta x} \leq 0.5$, at final time $T_f = 1$. Using the Lax-Friedrichs Method, we achieve the approximate solution curves shown in figure 3. As the figure shows, the nonlinear Lax-Friedrichs Method approximates the discontinuity well, though exhibits a large degree of smearing near the boundaries.

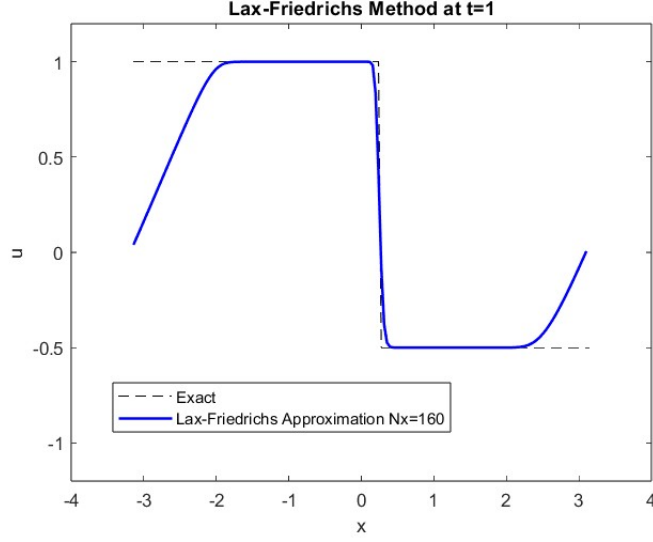


Figure 3: Approximate solution curve at time $t = 1$ of Burgers' Equation with the initial condition outlined in (1)

2.1.3 Riemann Problem 2

We now consider a second example by reversing the initial condition of Problem 1.

$$u_0(x) = \begin{cases} -0.5, & x \leq 0 \\ 1, & x > 0 \end{cases} \quad (2)$$

We can approximate this PDE along the interval $x \in [-\pi, \pi]$ using the spatial mesh size $N_x = 160$, with the CFL condition $\frac{\Delta t}{\Delta x} \leq 0.5$, at final time $T_f = 1$. Again using the Lax-Friedrichs approximation, we achieve the approximate solution curves shown in figure 4. Similarly to Problem 1, the approximate solution curve exhibits significant error near the left boundary.

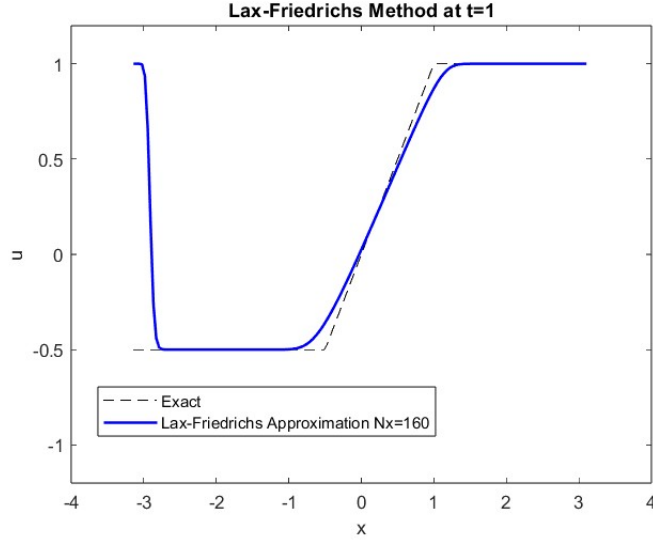


Figure 4: Approximate solution curve at time $t = 1$ of Burgers' Equation with the initial condition outlined in (2)

2.2 Two-Point Monotone Upwind Scheme for Conservative Laws (MUSCL)

2.2.1 Spatial Accuracy

We again consider the Inviscid Burgers' Equation

$$u_t + \left(\frac{1}{2}u^2\right)_x = 0$$

but we now approximate this PDE using MUSCL, a Total-Variation Decreasing (TVD) method, to ensure high-order accuracy in smooth regions while simultaneously handling discontinuities well. The Two-Point MUSCL Scheme is defined as

$$\bar{u}_j^{n+1} = \bar{u}_j^n - \frac{\Delta t}{\Delta x} (\hat{f}_{j+\frac{1}{2}} - \hat{f}_{j-\frac{1}{2}})$$

where \hat{f} represents the numerical flux function approximating $f(u) = \frac{1}{2}u^2$ and \bar{u}_j^n represents the function average of u inside cell j at time n .

We need to apply a high-order accuracy reconstruction method to approximate the slopes at both the left and right cell boundaries. We reconstruct the point values at the right cell boundaries $u_{j+\frac{1}{2}}^n$ from \bar{u}_j^n using the two methods below:

$$\begin{aligned} u_{j+\frac{1}{2}}^{(1)} &= \bar{u}_j^n + \frac{1}{2}(\bar{u}_j^n - \bar{u}_{j-1}^n) \\ u_{j+\frac{1}{2}}^{(2)} &= \bar{u}_j^n + \frac{1}{2}(\bar{u}_{j+1}^n - \bar{u}_j^n) \end{aligned}$$

We can define the difference at all times n between the point values at the right boundaries and the cell averages as

$$\tilde{u}_j^{(1)} = u_{j+\frac{1}{2}}^{(1)} - \bar{u}_j$$

$$\tilde{u}_j^{(2)} = u_{j+\frac{1}{2}}^{(2)} - \bar{u}_j$$

To smooth the approximation in order to better handle discontinuities we want to choose the smallest distance between \bar{u}_j and $(u_{j+\frac{1}{2}}^{(1,2)})$. We can thus define the **minmod** function as

$$\text{minmod}(a, b) = \begin{cases} \text{sign}(a) \min(|a|, |b|), & ab \geq 0 \\ 0, & ab < 0 \end{cases}$$

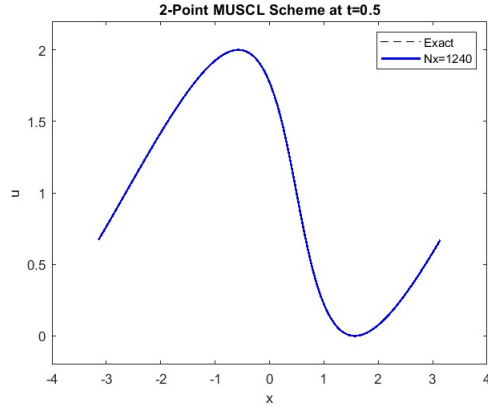
This can be used to minimize the difference between \bar{u}_j and $(u_{j+\frac{1}{2}}^{(1,2)})$ if we define the numerical flux \hat{f} as

$$\begin{aligned} \hat{f}_{j-\frac{1}{2}} &= f(\bar{u}_{j-1}^n + \text{minmod}(\tilde{u}_{j-1}^{(1)}, \tilde{u}_{j-1}^{(2)})) \\ \hat{f}_{j+\frac{1}{2}} &= f(\bar{u}_j^n + \text{minmod}(\tilde{u}_j^{(1)}, \tilde{u}_j^{(2)})) \end{aligned}$$

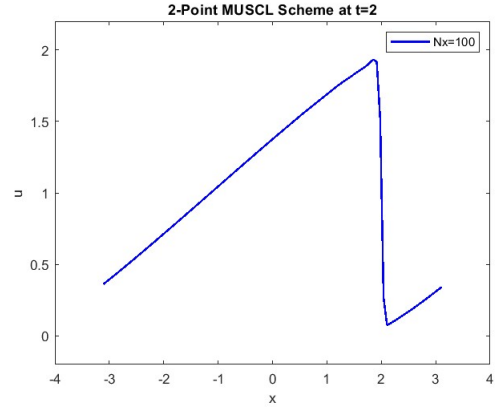
We consider the Inviscid Burgers' Equation along the interval $x \in [-\pi, \pi]$ with the initial condition $u_0(x) = \sin(x - \pi) + 1$, and can test the method's spatial accuracy before the breaking time $t_B = \min_u (\frac{-1}{\frac{d}{dx_0} f'(u_0(x_0))}) = 1$. The spatial accuracy of MUSCL is shown in Table 4 and the solution curves with $N_x = 100$ at times $t = 0.5$ and $t = 2$ after the breaking time $t_B = 1$ are shown in Figure 9.

N_x	L^1 Error	L^1 Order	L^2 Error	L^2 Order
40	4.32E-2	-	2.49E-2	-
80	1.63E-2	1.40	9.55E-3	1.38
160	3.63E-3	2.17	2.42E-3	1.98
320	7.87E-4	2.20	6.85E-4	1.82
640	2.72E-4	1.53	2.33E-4	1.56
1280	5.63E-5	2.27	7.17E-5	1.70

Table 4: 2-Point MUSCL spatial convergence table (converging to $\mathcal{O}(\Delta x^2)$) approximating Burgers' Equation with $u_0(x) = \sin(x - \pi) + 1$ at $T_f = 0.5$.



(a) Time $t = 0.5$ of Burgers' Equation



(b) Time $t = 2$ of Burgers' Equation

Figure 5: 2-Point MUSCL Solution Curve of Burgers' Equation with the initial condition $u_0(x) = \sin(x - \pi) + 1$ and $N_x = 100$ before and after breaking time $t_B = 1$

2.2.2 Riemann Problem 1

We can demonstrate how the Two-Point MUSCL method handles discontinuities by using it to approximate the Inviscid Burgers' Equation with discontinuous initial data.

$$u_0(x) = \begin{cases} 2, & x \leq 0 \\ 0, & x > 0 \end{cases} \quad (3)$$

We can approximate the Inviscid Burger's Equation along the interval $x \in [-\pi, \pi]$ using the spatial mesh size $N_x = 100$, with the CFL condition $\frac{\Delta t}{\Delta x^2} \leq 1$, at final time $T_f = 2$. Using the two-point MUSCL Method, we achieve the approximate solution curves shown in figure 6. As the figure shows, this method approximates the shock well, and only differs from the exact solution because of the periodic boundary conditions that occur in the approximation but are not accounted for in the exact solution.

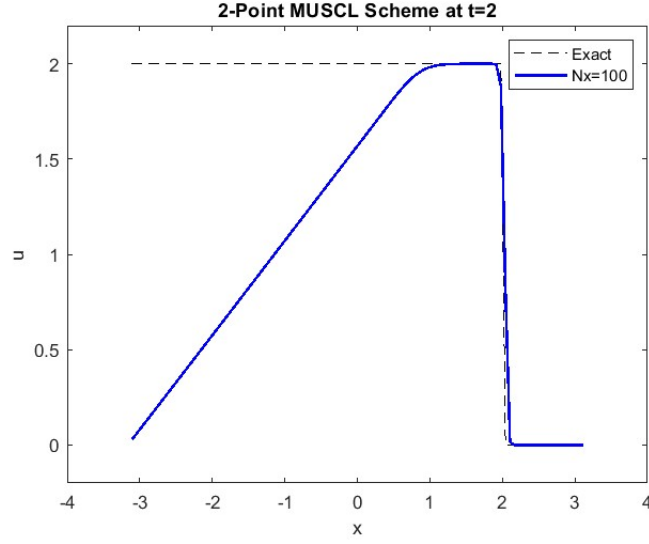


Figure 6: Approximate solution curve at time $t = 2$ of Burgers' Equation with the initial condition outlined in (3)

2.2.3 Riemann Problem 2

We now consider a second example by flipping Problem 1's initial data.

$$u_0(x) = \begin{cases} 0, & x \leq 0 \\ 2, & x > 0 \end{cases} \quad (4)$$

We approximate this PDE along the interval $x \in [-\pi, \pi]$ using the spatial mesh size $N_x = 100$, with the CFL condition $\frac{\Delta t}{\Delta x^2} \leq 1$, at final time $T_f = 2$. Again using the two-point MUSCL approximation, we achieve the approximate solution curve shown in figure 7.

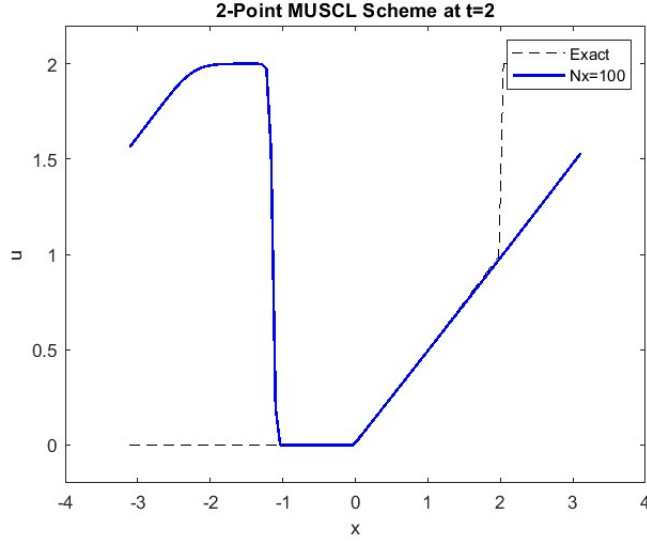


Figure 7: Approximate solution curve at time $t = 2$ of Burgers' Equation with the initial condition outlined in (4)

3 Week 4: 6/10/2024

3.1 MUSCL + RK2

3.1.1 Temporal and Spatial Accuracy

Osher's Theorem states that TVD methods are at most first-order accurate near smooth extrema. This explains why MUSCL does not converge perfectly in space to $\mathcal{O}(\Delta x^2)$ in either the L^1 or L^2 norms as demonstrated above in Week 3's Table 4. Additionally, this method is only first-order accurate in time, and we can achieve better temporal results by combining MUSCL with a two-stage Runge-Kutta method to achieve temporal accuracy of $\mathcal{O}(\Delta t^2)$. We now compute the solution u_j^{n+1} using two stages as follows:

$$\bar{u}_j^{(1)} = \bar{u}_j^n - \frac{\Delta t}{\Delta x} (\hat{f}_{j+\frac{1}{2}}(\bar{u}^n) - \hat{f}_{j-\frac{1}{2}}(\bar{u}^n))$$

$$\bar{u}_j^{n+1} = \frac{1}{2} \bar{u}_j^n + \frac{1}{2} \bar{u}_j^{(1)} - \frac{\Delta t}{2\Delta x} (\hat{f}_{j+\frac{1}{2}}(\bar{u}^{(1)}) - \hat{f}_{j-\frac{1}{2}}(\bar{u}^{(1)}))$$

We test the temporal convergence of MUSCL + RK2 using a temporal error convergence plot, shown in Figure 8. As shown, as the CFL coefficients λ increase (thus increasing Δt), the error increases at a rate corresponding to $\mathcal{O}(\Delta t^2)$ accuracy before blowing up after exceeding the CFL limit $\frac{\Delta t}{\Delta x} \leq \frac{1}{2}$.

We now test the spatial convergence of the method using time step of size $\Delta t \leq \Delta x$ because MUSCL + RK2 achieves $\mathcal{O}(\Delta t^2)$ temporal accuracy and thus we attain $\mathcal{O}(\Delta x^2)$ spatial accuracy even without the condition $\Delta t \leq \Delta x^2$ previously necessary in the original MUSCL algorithm from Week 3. The spatial accuracy (nearly converging to $\mathcal{O}(\Delta x^2)$) is shown in Table 5. Because MUSCL + RK2 is a TVD method, it remains constrained by Osher's Theorem, which states that any TVD method is at most first-order accurate near smooth extrema. Thus, the local minima and maxima in the sine wave "pollute" the second-order spatial accuracy, rendering MUSCL +

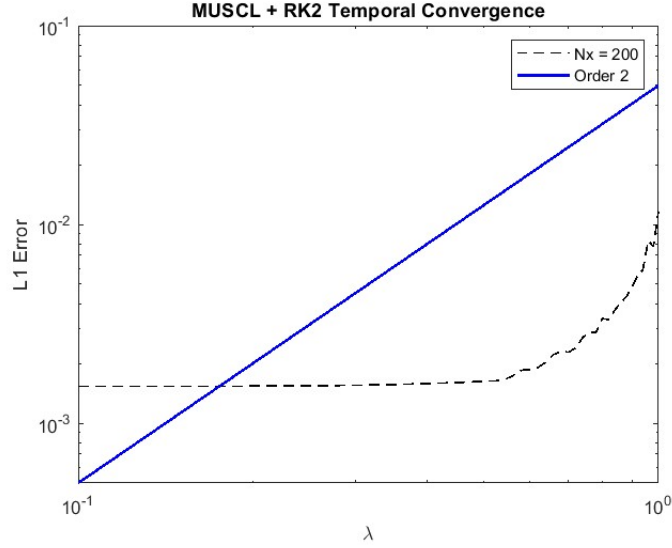


Figure 8: Temporal error plot converging to $\mathcal{O}(\Delta t^2)$ with spatial mesh size $N_x = 200$ approximating the linear advection equation with initial condition $u_0(x) = \sin x + 1$ at time $t = 0.5$.

RK2 slightly below $\mathcal{O}(\Delta x^2)$, especially in the L^2 norm, which, due to the squaring of the error terms, more heavily diminishes the second-order accuracy than the L^1 norm. This is why the L^1 norm converges to approximately 1.95 while the L^2 order only converges to approximately 1.64.

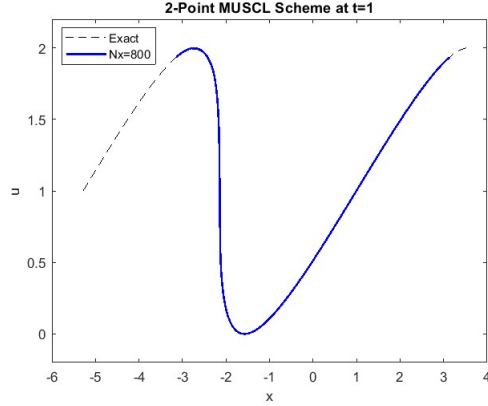
N_x	L^1 Error	L^1 Order	L^2 Error	L^2 Order
50	2.04E-02	-	1.22E-02	-
100	5.72E-03	1.84	3.96E-03	1.63
200	1.53E-03	1.90	1.27E-03	1.63
400	4.06E-04	1.91	4.10E-04	1.64
800	1.06E-04	1.94	1.32E-04	1.64

Table 5: MUSCL + RK2 spatial convergence table (converging to $\mathcal{O}(\Delta x^2)$) approximating the Linear Advection Equation with $u_0(x) = \sin x + 1$ at $T_f = 0.5$.

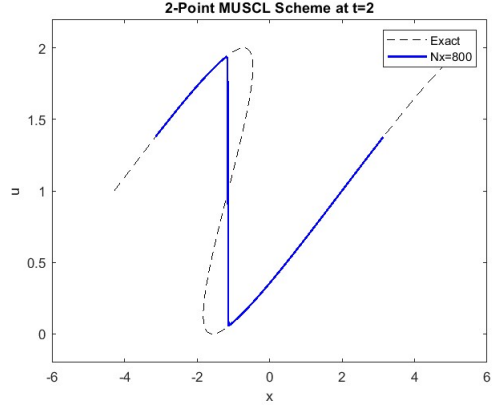
3.1.2 Test Problem 1: Burgers' Equation

Knowing that MUSCL + RK2 is $\mathcal{O}(\Delta t^2) + \mathcal{O}(\Delta x^2)$, we can use the algorithm to approximate the solution curves to the following Inviscid Burgers' Equation problem:

$$\begin{aligned}
 u_t + \left(\frac{1}{2} u^2 \right)_x &= 0 \\
 u_0(x) &= \sin x + 1
 \end{aligned} \tag{5}$$



(a) Approximate solution curve at time $t = 1$



(b) Approximate solution curve at time $t = 2$

Figure 9: 2-Point MUSCL + RK2 Solution Curve of Burgers' Equation with the initial condition $u_0(x) = \sin(x) + 1$ and $N_x = 800$ both at and after breaking time $t_B = 1$

We see that the theoretical exact solution curve traces back over itself (simulating a wave that never "breaks") while the numerical solution correctly approximates the shock without any oscillations or smearing due to its TVD nature.

3.2 WENO

To achieve higher order accuracy than using linear reconstruction to approximate node values from cell averages, we can use linear combinations of the three third-order reconstruction polynomials $P^{(i)}(x_{j+\frac{1}{2}}) \approx u_{j+\frac{1}{2}}^{(i)}$ – centered around the intervals $I_i = \{\bar{u}_{i-2}, \bar{u}_{i-1}, \bar{u}_i\}$, $i = 0, 1, 2$ – to achieve $\mathcal{O}(\Delta x^5)$ accuracy with the correct weights ω_i .

$$u_{j+\frac{1}{2}} = \omega_1 u_{j+\frac{1}{2}}^{(1)} + \omega_2 u_{j+\frac{1}{2}}^{(2)} + \omega_3 u_{j+\frac{1}{2}}^{(3)}$$

We obtain the third-order point-value reconstructions $u_{j+\frac{1}{2}}^{(i)}$ using linear combinations of surrounding cell averages inside the respective interval I_i . We can use the table of linear reconstruction weights $c_{i,j}$ and the formula $u_{j+\frac{1}{2}}^{(i)} = \sum_{k=0}^2 c_{i,k} \bar{u}_{j+k}$ to reconstruct the point values at the right boundaries from the cell averages. Note that if we are finding the right-limit left boundary values, we use $i = -1, 0, 1$, whereas if we want to compute the left-limit right-boundary values, we use $i = 0, 1, 2$.

	j=0	j=1	j=2
$i = -1$	$\frac{11}{6}$	$-\frac{7}{6}$	$\frac{1}{3}$
$i = 0$	$\frac{1}{3}$	$\frac{5}{6}$	$-\frac{1}{6}$
$i = 1$	$-\frac{1}{6}$	$\frac{5}{6}$	$\frac{1}{3}$
$i = 2$	$\frac{1}{3}$	$-\frac{7}{6}$	$\frac{11}{6}$

Table 6: Table of linear reconstruction weights $c_{i,j}$ approximating the point value $u_{j+\frac{1}{2}}^{(i)}$ using the formula $u_{j+\frac{1}{2}}^{(i)} = \sum_{k=0}^2 c_{i,k} \bar{u}_{j+k}$

We find the weights ω_i via

$$\omega_i = \frac{\alpha_i}{\sum_{k=1}^3 \alpha_k}, \quad i = 1, 2, 3$$

where

$$\alpha = \frac{d_i}{(\epsilon + \beta_i)^2}, \quad i = 1, 2, 3$$

and β_i indicates the smoothness (lower = smoother), $\epsilon = 10^{-6}$ to prevent division by 0, and d_i is given by

$$d_1 = \frac{3}{10}, \quad d_2 = \frac{3}{5}, \quad d_3 = \frac{1}{10}$$

β_i is derived from the cell averages using the following formulae

$$\begin{aligned} \beta_1 &= \frac{13}{12}(\bar{u}_{i-2} - 2\bar{u}_{i-1} + \bar{u}_i)^2 + \frac{1}{4}(\bar{u}_{i-2} - 4\bar{u}_{i-1} + 3\bar{u}_i)^2 \\ \beta_2 &= \frac{13}{12}(\bar{u}_{i-1} - 2\bar{u}_i + \bar{u}_{i+1})^2 + \frac{1}{4}(\bar{u}_{i-1} - \bar{u}_{i+1})^2 \\ \beta_3 &= \frac{13}{12}(\bar{u}_i - 2\bar{u}_{i+1} + \bar{u}_{i+2})^2 + \frac{1}{4}(3\bar{u}_i - 4\bar{u}_{i+1} + \bar{u}_{i+2})^2 \end{aligned}$$

Note that this assumes we are determining the left-limit node values at the right boundaries $u_{j+\frac{1}{2}}^-$. Assuming periodicity, to determine the right-limit point values at the left boundaries $u_{j-\frac{1}{2}}^+$, we need to reverse the weights d_i such that

$$d_1 = \frac{1}{10}, \quad d_2 = \frac{3}{5}, \quad d_3 = \frac{3}{10}$$

and similarly alter the linear reconstruction weights in Table 6 as stated above.

3.2.1 Spatial Accuracy

We can test this algorithm, implemented in MATLAB, using the smooth function $u(x) = \sin x$. We find that evaluating both $u_{j+\frac{1}{2}}^-$ and $u_{j-\frac{1}{2}}^+$, we achieve exactly the same error values, both converging to $\mathcal{O}(\Delta x^5)$ as shown below in Table 7.

N_x	L^1 Error	L^1 Order	L^2 Error	L^2 Order
40	4.09E-05	-	1.90E-05	-
80	1.35E-06	4.92	6.10E-07	4.96
160	4.30E-08	4.97	1.92E-08	4.99
320	1.35E-09	5.00	6.00E-10	5.00
640	4.14E-11	5.02	1.86E-11	5.02

Table 7: WENO5 spatial convergence table (converging to $\mathcal{O}(\Delta x^5)$) approximating $u(x) = \sin x$.

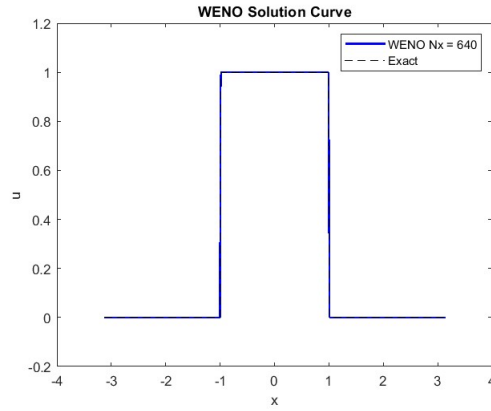
If we temporarily eliminate the WENO weighting, simply setting $\omega_i = d_i$, we still can achieve fifth-order accuracy in smooth regions, but we lose high accuracy near discontinuities. To demonstrate, the spatial error convergence tested on the smooth function $\sin x$ with $\omega_i = d_i$ is shown below in Table 8. However, when we eliminate the WENO weighting while approximating the Heaviside step function, we observe spurious oscillations, threatening stability (shown below in Figure 10b).

N_x	L^1 Error	L^1 Order	L^2 Error	L^2 Order
40	6.36E-06	-	2.81E-06	-
80	1.99E-07	5.00	8.82E-08	5.00
160	6.22E-09	5.00	2.76E-09	5.00
320	1.95E-10	5.00	8.62E-11	5.00
640	6.08E-12	5.00	2.69E-12	5.00

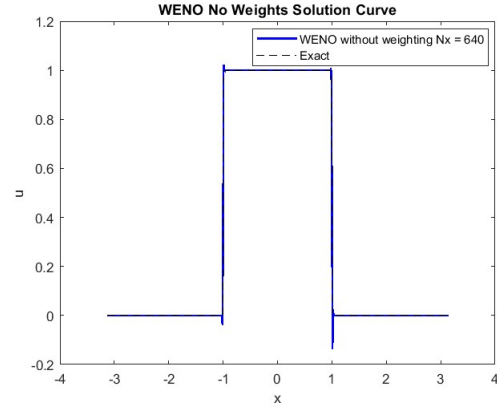
Table 8: WENO5 spatial convergence table without weights (converging to $\mathcal{O}(\Delta x^5)$) approximating $u(x) = \sin x$.

3.2.2 Test on Heaviside Step Function

We can now test WENO on the Heaviside step function, using a spatial mesh size $N_x = 640$. As shown in Figure 10a, when we include the WENO weighting we observe oscillation control near discontinuities. However, as shown in Figure 10b, when we eliminate these weights, setting $\omega_i = d_i$, we observe oscillations near the discontinuities.



(a) Approximate Heaviside solution curve using WENO



(b) Approximate Heaviside solution curve using "weightless" WENO

Figure 10: Comparison of two approximations of the Heaviside step function using spatial mesh size $N_x = 640$ with and without the WENO weights

We conclude that WENO works well to eliminate spurious oscillations near discontinuities while circumventing the TVD disadvantage of maximum first-order accuracy near smooth extrema.

4 Week 5: 1D WENO5 Finite Difference Solver

This week, we combine WENO5 with both finite volume and finite difference methods to solve one-dimensional, first-order PDEs such as Burgers' Equation, and the Linear Advection equation.

4.1 Finite Volume Method

Using the finite volume method, we construct a mini library of MATLAB scripts to combine Lax-Friedrich's Flux, WENO5, and various strong stability-preserving Runge-Kutta methods (SSP-RK1, SSP-Rk2, or SSP-RK3) to achieve $\mathcal{O}(\Delta x^5)$ spatial accuracy and $\mathcal{O}(\Delta t)$, $\mathcal{O}(\Delta t^2)$, or $\mathcal{O}(\Delta t^3)$ temporal accuracy depending on the Runge-Kutta method. The spatial accuracy of these three methods is shown below for four test cases: Burgers' Equation, Linear Advection, and variable coefficient equations in space and time. We verify the spatial accuracy for these test cases at the final time $T_f = 0.5$ with a timestep size $\Delta t = 0.3(\Delta x)$ to satisfy the CFL condition $\Delta t \leq \Delta x$.

4.1.1 Test Case 1: Burgers' Equation

We first verify this algorithm's spatial accuracy on Burgers' Equation

$$u_t + \left(\frac{u^2}{2} \right)_x = 0, \quad x \in [0, 2\pi]$$

with the initial condition

$$u_0(x) = \sin x$$

at the final time

$$T_f = 0.5$$

where the exact solution is defined by the implicit equation

$$u(x, t) = u_0(x - tu(x, t))$$

Tables 9, 10, and 11 show convergence of WENO5+SSP-RK1, RK2, and RK3, respectively converging to $\mathcal{O}(\Delta t)$, $\mathcal{O}(\Delta t^2)$, and $\mathcal{O}(\Delta t^3)$ in both L^1 and L^2 norms.

N_x	L^1 Error	L^1 Order	L^2 Error	L^2 Order
40	3.67E-02	-	1.83E-02	-
80	1.88E-02	0.97	9.33E-03	0.97
160	9.37E-03	1.00	4.68E-03	1.00
320	4.70E-03	1.00	2.35E-03	0.99
640	2.35E-03	1.00	1.17E-03	1.00

Table 9: WENO5+SSP-RK1 spatial convergence table (converging to $\mathcal{O}(\Delta t)$) approximating Burgers' Equation with initial condition $u_0(x) = \sin x$, timestep size $\Delta t = 0.3(\Delta x)$, at final time $T_f = 0.5$.

N_x	L^1 Error	L^1 Order	L^2 Error	L^2 Order
40	1.41E-03	-	7.59E-04	-
80	2.98E-04	2.25	1.59E-04	2.26
160	7.20E-05	2.05	3.85E-05	2.04
320	1.80E-05	2.00	9.68E-06	1.99
640	4.77E-06	1.92	2.57E-06	1.91

Table 10: WENO5+SSP-RK2 spatial convergence table (converging to $\mathcal{O}(\Delta t^2)$) approximating Burgers' Equation with initial condition $u_0(x) = \sin x$, timestep size $\Delta t = 0.3(\Delta x)$, at final time $T_f = 0.5$.

N_x	L^1 Error	L^1 Order	L^2 Error	L^2 Order
40	3.98E-04	-	3.45E-04	-
80	1.96E-05	4.34	1.72E-05	4.33
160	1.63E-06	3.59	1.22E-06	3.82
320	8.92E-07	0.87	8.78E-07	0.47
640	8.64E-07	0.04	9.43E-07	-0.10

Table 11: WENO5+SSP-RK3 spatial convergence table (converging to $\mathcal{O}(\Delta t^3)$) approximating Burgers' Equation with initial condition $u_0(x) = \sin x$, timestep size $\Delta t = 0.3(\Delta x)$, at final time $T_f = 0.5$.

We can also plot the solution curve for Burgers' Equation using WENO5+RK3 to illustrate adequate post-shock approximation and reduction of spurious oscillations near discontinuities. The solution curve and the exact theoretical solution are shown below in Figure 11.

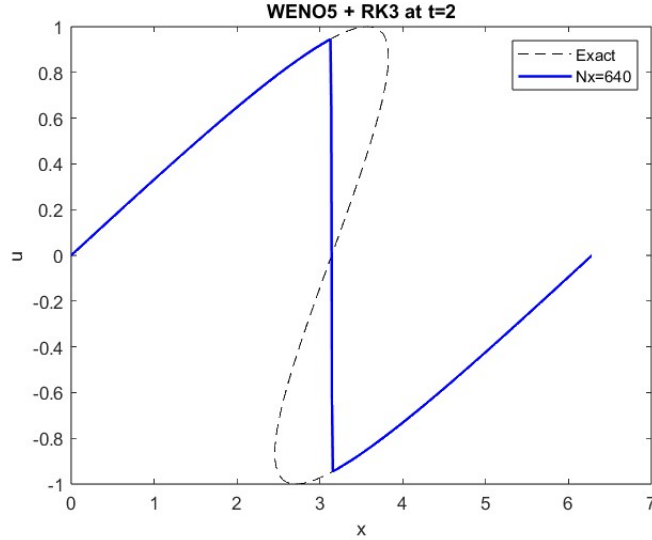


Figure 11: Solution curve of Burgers' Equation with initial condition $u_0(x) = \sin x$ at final time $T_f = 2$ after the breaking time $T_B = 1$ with spatial mesh size $N_x = 640$.

4.1.2 Test Case 2: Linear Advection

We next test WENO5+RK1/2/3 on the Linear Advection Equation

$$u_t + u_x = 0, \quad x \in [0, 2\pi]$$

with the initial condition

$$u_0(x) = \sin x$$

at the final time

$$T_f = 0.5$$

where the exact solution is

$$u(x, t) = u_0(x - t)$$

Tables 12, 13, and 14 show convergence of WENO5+SSP-RK1, RK2, and RK3, respectively converging to $\mathcal{O}(\Delta t)$, $\mathcal{O}(\Delta t^2)$, and $\mathcal{O}(\Delta t^3)$ in both L^1 and L^2 norms.

N_x	L^1 Error	L^1 Order	L^2 Error	L^2 Order
40	4.63E-02	-	2.05E-02	-
80	2.34E-02	0.98	1.04E-02	0.98
160	1.17E-02	1.00	5.20E-03	1.00
320	5.89E-03	0.99	2.61E-03	0.99
640	2.94E-03	1.00	1.30E-03	1.00

Table 12: WENO5+SSP-RK1 spatial convergence table (converging to $\mathcal{O}(\Delta t)$) approximating the Linear Advection Equation with initial condition $u_0(x) = \sin x$, timestep size $\Delta t = 0.3(\Delta x)$, at final time $T_f = 0.5$.

N_x	L^1 Error	L^1 Order	L^2 Error	L^2 Order
40	7.14E-04	-	3.15E-04	-
80	1.83E-04	1.96	8.12E-05	1.96
160	4.59E-05	2.00	2.03E-05	2.00
320	1.15E-05	1.99	5.11E-06	1.99
640	2.89E-06	2.00	1.28E-06	2.00

Table 13: WENO5+SSP-RK2 spatial convergence table (converging to $\mathcal{O}(\Delta t^2)$) approximating the Linear Advection Equation with initial condition $u_0(x) = \sin x$, timestep size $\Delta t = 0.3(\Delta x)$, at final time $T_f = 0.5$.

N_x	L^1 Error	L^1 Order	L^2 Error	L^2 Order
40	3.13E-05	-	1.44E-05	-
80	1.78E-06	4.14	7.92E-07	4.19
160	1.57E-07	3.50	6.95E-08	3.51
320	1.77E-08	3.15	7.82E-09	3.15
640	2.14E-09	3.04	9.50E-10	3.04

Table 14: WENO5+SSP-RK3 spatial convergence table (converging to $\mathcal{O}(\Delta t^3)$) approximating the Linear Advection Equation with initial condition $u_0(x) = \sin x$, timestep size $\Delta t = 0.3(\Delta x)$, at final time $T_f = 0.5$.

The solution curve and the exact theoretical solution for the Linear Advection Equation with an initial condition of the Heaviside Step Function defined below in Equation 6 at time $T_f = 2$ are shown below in Figure 11. The algorithm handles discontinuities well, damping spurious oscillations near the discontinuity.

$$u_0(x) = \begin{cases} 0, & x \leq 1 \\ 1, & x > 1 \end{cases} \quad (6)$$

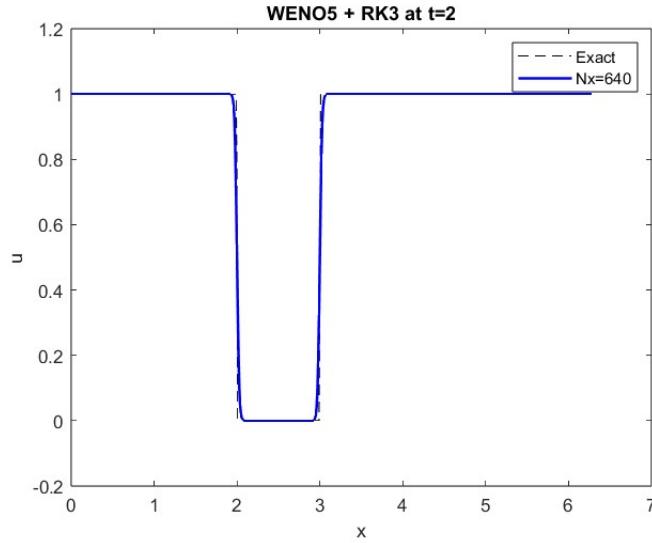


Figure 12: Solution curve of the Linear Advection Equation with the Heaviside step function initial condition at final time $T_f = 2$ with spatial mesh size $N_x = 640$.

4.1.3 Test Case 3: Variable Coefficient in Space

We now test WENO5+RK1/2/3 on the variable coefficient equation

$$u_t + (u \sin x)_x = 0, \quad x \in [0, 2\pi]$$

with the initial condition

$$u_0(x) = 1$$

at the final time

$$T_f = 0.5$$

where the exact solution is

$$u(x, t) = \frac{\sin(2 \arctan(e^{-t} \tan(x/2)))}{\sin(x)}$$

Tables 15, 16, and 17 show convergence of WENO5+SSP-RK1, RK2, and RK3, respectively converging to $\mathcal{O}(\Delta t)$, $\mathcal{O}(\Delta t^2)$, and $\mathcal{O}(\Delta t^3)$ in both L^1 and L^2 norms.

N_x	L^1 Error	L^1 Order	L^2 Error	L^2 Order
40	4.62E-02	-	2.16E-02	-
80	2.35E-02	0.98	1.10E-02	0.97
160	1.17E-02	1.00	5.51E-03	1.00
320	5.89E-03	0.99	2.77E-03	0.99
640	2.94E-03	1.00	1.38E-03	1.00

Table 15: WENO5+SSP-RK1 spatial convergence table (converging to $\mathcal{O}(\Delta t)$) approximating the variable coefficient equation $u_t + (u \sin x)_x = 0$ with initial condition $u_0(x) = 1$, timestep size $\Delta t = 0.3(\Delta x)$, at final time $T_f = 0.5$.

N_x	L^1 Error	L^1 Order	L^2 Error	L^2 Order
40	1.13E-03	-	5.40E-04	-
80	2.84E-04	2.00	1.36E-04	1.99
160	7.09E-05	2.00	3.41E-05	2.00
320	1.78E-05	1.99	8.58E-06	1.99
640	4.46E-06	2.00	2.15E-06	2.00

Table 16: WENO5+SSP-RK2 spatial convergence table (converging to $\mathcal{O}(\Delta t^2)$) approximating the variable coefficient equation $u_t + (u \sin x)_x = 0$ with initial condition $u_0(x) = 1$, timestep size $\Delta t = 0.3(\Delta x)$, at final time $T_f = 0.5$.

N_x	L^1 Error	L^1 Order	L^2 Error	L^2 Order
40	6.03E-05	-	4.18E-05	-
80	4.34E-06	3.79	2.30E-06	4.18
160	4.64E-07	3.23	2.31E-07	3.32
320	5.71E-08	3.02	2.87E-08	3.01
640	7.12E-09	3.00	3.60E-09	3.00

Table 17: WENO5+SSP-RK3 spatial convergence table (converging to $\mathcal{O}(\Delta t^3)$) approximating the variable coefficient equation $u_t + (u \sin x)_x = 0$ with initial condition $u_0(x) = 1$, timestep size $\Delta t = 0.3(\Delta x)$, at final time $T_f = 0.5$.

The solution curve and the exact theoretical solution for the above variable coefficient equation at time $T_f = 2$ are shown below in Figure 13.

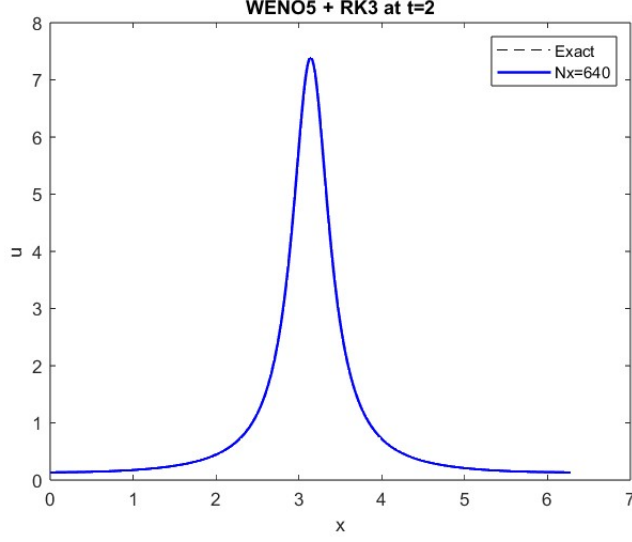


Figure 13: Solution curve of the variable coefficient equation $u_t + (u \sin x)_x = 0$ with initial condition $u_0(x) = \sin x$ at final time $T_f = 2$ with spatial mesh size $N_x = 640$.

4.1.4 Test Case 4: Variable Coefficient in Time

Finally, we analyze the spatial accuracy of WENO5+RK1/2/3 on the variable coefficient equation

$$u_t + \left(\frac{u}{1+t} \right)_x = 0, \quad x \in [0, 2\pi]$$

with the initial condition

$$u_0(x) = e^{-5(x-\pi)^2}$$

at the final time

$$T_f = 0.5$$

where the exact solution is

$$u(x, t) = \exp[-5(x - \log(t+1) - \pi)^2]$$

Tables 18, 19, and 20 show convergence of WENO5+SSP-RK1, RK2, and RK3, respectively converging to $\mathcal{O}(\Delta t)$, $\mathcal{O}(\Delta t^2)$, and $\mathcal{O}(\Delta t^3)$ in both L^1 and L^2 norms.

N_x	L^1 Error	L^1 Order	L^2 Error	L^2 Order
40	5.24E-02	-	4.67E-02	-
80	3.12E-02	0.75	2.69E-02	0.80
160	1.57E-02	0.99	1.34E-02	1.00
320	7.80E-03	1.01	6.66E-03	1.01
640	3.88E-03	1.01	3.31E-03	1.01

Table 18: WENO5+SSP-RK1 spatial convergence table (converging to $\mathcal{O}(\Delta t)$) approximating the variable coefficient equation $u_t + \left(\frac{u}{1+t}\right)_x = 0$ with initial condition $u_0(x) = e^{-5(x-\pi)^2}$, timestep size $\Delta t = 0.3(\Delta x)$, at final time $T_f = 0.5$.

N_x	L^1 Error	L^1 Order	L^2 Error	L^2 Order
40	1.07E-02	-	8.98E-03	-
80	1.04E-03	3.36	1.05E-03	3.10
160	2.49E-04	2.06	2.14E-04	2.29
320	6.25E-05	1.99	5.40E-05	1.99
640	1.56E-05	2.00	1.35E-05	2.00

Table 19: WENO5+SSP-RK2 spatial convergence table (converging to $\mathcal{O}(\Delta t^2)$) approximating the variable coefficient equation $u_t + \left(\frac{u}{1+t}\right)_x = 0$ with initial condition $u_0(x) = e^{-5(x-\pi)^2}$, timestep size $\Delta t = 0.3(\Delta x)$, at final time $T_f = 0.5$.

N_x	L^1 Error	L^1 Order	L^2 Error	L^2 Order
40	1.13E-02	-	9.78E-03	-
80	8.45E-04	3.74	7.94E-04	3.62
160	3.54E-05	4.58	3.29E-05	4.59
320	1.40E-06	4.66	1.32E-06	4.64
640	7.95E-08	4.14	7.64E-08	4.11

Table 20: WENO5+SSP-RK3 spatial convergence table (exceeding $\mathcal{O}(\Delta t^3)$) approximating the variable coefficient equation $u_t + \left(\frac{u}{1+t}\right)_x = 0$ with initial condition $u_0(x) = e^{-5(x-\pi)^2}$, timestep size $\Delta t = 0.3(\Delta x)$, at final time $T_f = 0.5$.

The solution curve and the exact theoretical solution for the second variable coefficient equation at time $T_f = 2$ are shown below in Figure 14.

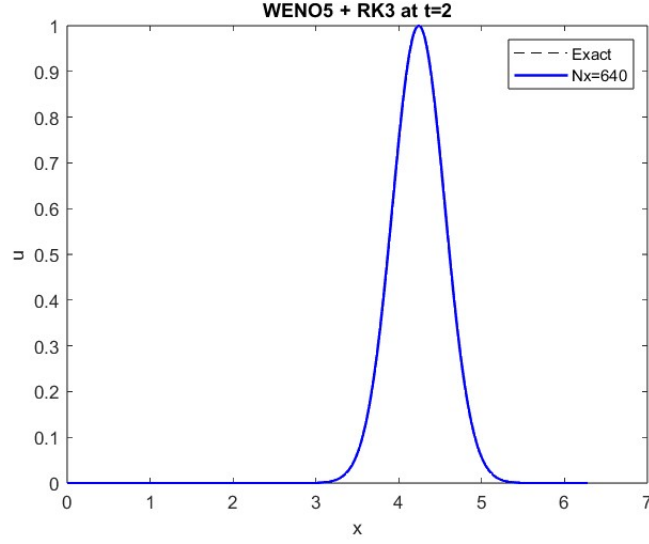


Figure 14: Solution curve of the variable coefficient equation $u_t + \left(\frac{u}{1+t}\right)_x = 0$ with initial condition $u_0(x) = \sin x$ at final time $T_f = 2$ with spatial mesh size $N_x = 640$.

4.2 Finite Differences Method

We now remake the mini library to use the finite differences method, rather than finite volume. Therefore, we compute the solution $u(x, t)$ at cell midpoints rather than across entire cells.

4.2.1 Test Case 1: Burgers' Equation

We first analyze the spatial accuracy of WENO5+RK1/2/3 for finite differences Burgers' Equation

$$u_t + \left(\frac{u^2}{2}\right)_x = 0, \quad x \in [0, 2\pi]$$

with the initial condition

$$u_0(x) = \sin x$$

at the final time

$$T_f = 0.5$$

where the exact solution is defined by the implicit equation

$$u(x, t) = u_0(x - tu(x, t))$$

Tables 21, 22, and 23 show the spatial convergence of the finite difference WENO5+SSP-RK1, RK2, and RK3, respectively converging to $\mathcal{O}(\Delta t)$, $\mathcal{O}(\Delta t^2)$, and $\mathcal{O}(\Delta t^3)$ in both L^1 and L^2 norms.

N_x	L^1 Error	L^1 Order	L^2 Error	L^2 Order
40	3.72E-02	-	1.84E-02	-
80	1.87E-02	0.99	9.33E-03	0.98
160	9.38E-03	1.00	4.67E-03	1.00
320	4.70E-03	1.00	2.35E-03	0.99
640	2.35E-03	1.00	1.17E-03	1.00

Table 21: Finite Differences WENO5+SSP-RK1 spatial convergence table (converging to $\mathcal{O}(\Delta t)$) approximating Burgers' Equation with initial condition $u_0(x) = \sin x$, timestep size $\Delta t = 0.3(\Delta x)$, at final time $T_f = 0.5$.

N_x	L^1 Error	L^1 Order	L^2 Error	L^2 Order
40	1.40E-03	-	7.89E-04	-
80	2.91E-04	2.27	1.55E-04	2.35
160	7.20E-05	2.01	3.85E-05	2.01
320	1.80E-05	2.00	9.67E-06	1.99
640	4.55E-06	1.98	2.44E-06	1.99

Table 22: Finite Differences WENO5+SSP-RK2 spatial convergence table (converging to $\mathcal{O}(\Delta t^2)$) approximating Burgers' Equation with initial condition $u_0(x) = \sin x$, timestep size $\Delta t = 0.3(\Delta x)$, at final time $T_f = 0.5$.

N_x	L^1 Error	L^1 Order	L^2 Error	L^2 Order
40	6.71E-04	-	4.50E-04	-
80	2.40E-05	4.80	1.78E-05	4.66
160	1.47E-06	4.03	9.27E-07	4.26
320	9.26E-08	3.99	5.32E-08	4.12
640	7.37E-08	0.33	7.81E-08	-0.55

Table 23: Finite Differences WENO5+SSP-RK3 spatial convergence table (converging to $\mathcal{O}(\Delta t^3)$) approximating Burgers' Equation with initial condition $u_0(x) = \sin x$, timestep size $\Delta t = 0.3(\Delta x)$, at final time $T_f = 0.5$.

We now plot Burgers' Equation's solution curve and exact theoretical solution using WENO5+RK3 to illustrate adequate post-shock approximation and reduction of spurious oscillations near discontinuities. The solution curve and the exact theoretical solution are shown below in Figure 15.

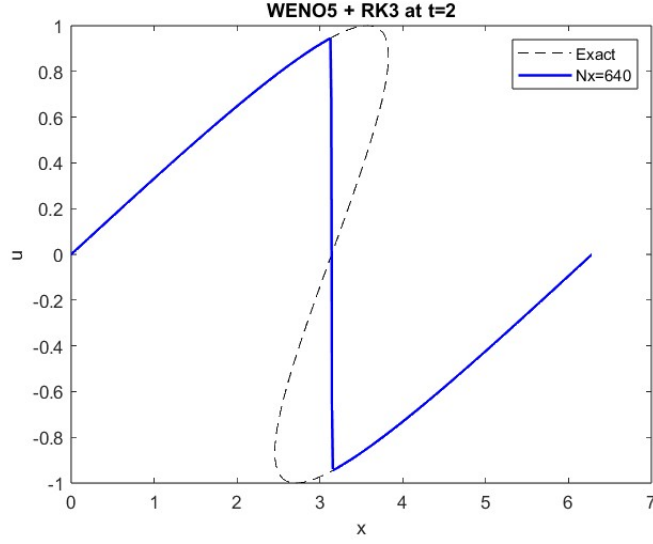


Figure 15: Solution curve of Burgers' Equation with initial condition $u_0(x) = \sin x$ at final time $T_f = 2$ with spatial mesh size $N_x = 640$.

4.2.2 Test Case 2: Linear Advection

We first analyze the spatial accuracy of Finite Differences WENO5+RK1/2/3 for the Linear Advection Equation

$$u_t + u_x = 0, \quad x \in [0, 2\pi]$$

with the initial condition

$$u_0(x) = \sin x$$

at the final time

$$T_f = 0.5$$

where the exact solution is defined by the equation

$$u(x, t) = u_0(x - t)$$

Tables 24, 25, and 26 show the spatial convergence of the finite difference WENO5+SSP-RK1, RK2, and RK3, respectively converging to $\mathcal{O}(\Delta t)$, $\mathcal{O}(\Delta t^2)$, and $\mathcal{O}(\Delta t^3)$ in both L^1 and L^2 norms.

N_x	L^1 Error	L^1 Order	L^2 Error	L^2 Order
40	5.04E-02	-	2.23E-02	-
80	2.45E-02	1.04	1.08E-02	1.04
160	1.20E-02	1.03	5.31E-03	1.03
320	5.95E-03	1.01	2.64E-03	1.01
640	2.96E-03	1.01	1.31E-03	1.01

Table 24: Finite Differences WENO5+SSP-RK1 spatial convergence table (converging to $\mathcal{O}(\Delta t)$) approximating the Linear Advection Equation with initial condition $u_0(x) = \sin x$, timestep size $\Delta t = 0.3(\Delta x)$, at final time $T_f = 0.5$.

N_x	L^1 Error	L^1 Order	L^2 Error	L^2 Order
40	7.15E-04	-	3.15E-04	-
80	1.83E-04	1.96	8.12E-05	1.96
160	4.59E-05	2.00	2.03E-05	2.00
320	1.15E-05	1.99	5.11E-06	1.99
640	2.89E-06	2.00	1.28E-06	2.00

Table 25: Finite Differences WENO5+SSP-RK2 spatial convergence table (converging to $\mathcal{O}(\Delta t^2)$) approximating the Linear Advection Equation with initial condition $u_0(x) = \sin x$, timestep size $\Delta t = 0.3(\Delta x)$, at final time $T_f = 0.5$.

N_x	L^1 Error	L^1 Order	L^2 Error	L^2 Order
40	3.13E-05	-	1.44E-05	-
80	1.78E-06	4.14	7.92E-07	4.19
160	1.57E-07	3.50	6.95E-08	3.51
320	1.77E-08	3.15	7.82E-09	3.15
640	2.14E-09	3.04	9.50E-10	3.04

Table 26: Finite Differences WENO5+SSP-RK3 spatial convergence table (converging to $\mathcal{O}(\Delta t^3)$) approximating the Linear Advection Equation with initial condition $u_0(x) = \sin x$, timestep size $\Delta t = 0.3(\Delta x)$, at final time $T_f = 0.5$.

We now plot the solution curve and exact theoretical solution of the Linear Advection Equation with the Heaviside Step Function initial condition shown below in Equation 7 using the finite differences WENO5+RK3 algorithm to illustrate spurious oscillation control near discontinuities. The solution curve and the exact theoretical solution are shown below in Figure 16.

$$u_0(x) = \begin{cases} 0, & x \leq 1 \\ 1, & x > 1 \end{cases} \quad (7)$$

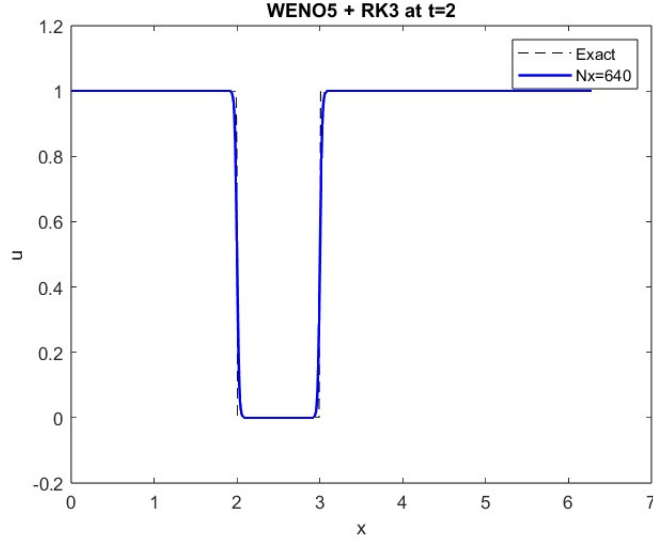


Figure 16: Solution curve of the Linear Advection Equation with the Heaviside Step Function initial condition at final time $T_f = 2$ with spatial mesh size $N_x = 640$.

4.2.3 Test Case 3: Variable Spatial Coefficient

We now test the finite differences WENO5+RK1/2/3 on the variable coefficient equation

$$u_t + (u \sin x)_x = 0, \quad x \in [0, 2\pi]$$

with the initial condition

$$u_0(x) = 1$$

at the final time

$$T_f = 0.5$$

where the exact solution is

$$u(x, t) = \frac{\sin(2 \arctan(e^{-t} \tan(x/2)))}{\sin(x)}$$

Tables 27, 28, and 29 show the spatial convergence of the finite difference WENO5+SSP-RK1, RK2, and RK3, respectively converging to $\mathcal{O}(\Delta t)$, $\mathcal{O}(\Delta t^2)$, and $\mathcal{O}(\Delta t^3)$ in both L^1 and L^2 norms.

N_x	L^1 Error	L^1 Order	L^2 Error	L^2 Order
40	4.55E-02	-	2.10E-02	-
80	2.32E-02	0.97	1.08E-02	0.95
160	1.17E-02	0.99	5.47E-03	0.99
320	5.87E-03	0.99	2.76E-03	0.99
640	2.94E-03	1.00	1.38E-03	1.00

Table 27: Finite Differences WENO5+SSP-RK1 spatial convergence table (converging to $\mathcal{O}(\Delta t)$) approximating the variable coefficient equation $u_t + \left(\frac{u}{1+t}\right)_x = 0$ with initial condition $u_0(x) = 1$, timestep size $\Delta t = 0.3(\Delta x)$, at final time $T_f = 0.5$.

N_x	L^1 Error	L^1 Order	L^2 Error	L^2 Order
40	1.14E-03	-	5.55E-04	-
80	2.84E-04	2.01	1.36E-04	2.03
160	7.09E-05	2.00	3.41E-05	2.00
320	1.78E-05	1.99	8.58E-06	1.99
640	4.46E-06	2.00	2.15E-06	2.00

Table 28: Finite Differences WENO5+SSP-RK2 spatial convergence table (converging to $\mathcal{O}(\Delta t^2)$) approximating the variable coefficient equation $u_t + \left(\frac{u}{1+t}\right)_x = 0$ with initial condition $u_0(x) = 1$, timestep size $\Delta t = 0.3(\Delta x)$, at final time $T_f = 0.5$.

N_x	L^1 Error	L^1 Order	L^2 Error	L^2 Order
40	1.81E-04	-	1.21E-04	-
80	7.94E-06	4.51	5.08E-06	4.58
160	5.57E-07	3.83	2.95E-07	4.10
320	5.90E-08	3.24	2.95E-08	3.32
640	7.17E-09	3.04	3.62E-09	3.03

Table 29: Finite Differences WENO5+SSP-RK3 spatial convergence table (converging to $\mathcal{O}(\Delta t^3)$) approximating the variable coefficient equation $u_t + \left(\frac{u}{1+t}\right)_x = 0$ with initial condition $u_0(x) = 1$, timestep size $\Delta t = 0.3(\Delta x)$, at final time $T_f = 0.5$.

4.2.4 Test Case 4: Variable Coefficient in Time

Finally, we analyze the spatial accuracy of the finite differences WENO5+RK1/2/3 on the variable coefficient equation

$$u_t + \left(\frac{u}{1+t}\right)_x = 0, \quad x \in [0, 2\pi]$$

with the initial condition

$$u_0(x) = e^{-5(x-\pi)^2}$$

at the final time

$$T_f = 0.5$$

where the exact solution is

$$u(x, t) = \exp[-5(x - \log(t + 1) - \pi)^2]$$

Tables 30, 31, and 32 show convergence of WENO5+SSP-RK1, RK2, and RK3, respectively converging to $\mathcal{O}(\Delta t)$, $\mathcal{O}(\Delta t^2)$, and $\mathcal{O}(\Delta t^3)$ in both L^1 and L^2 norms.

N_x	L^1 Error	L^1 Order	L^2 Error	L^2 Order
40	6.08E-02	-	5.40E-02	-
80	3.32E-02	0.87	2.87E-02	0.91
160	1.62E-02	1.04	1.38E-02	1.05
320	7.92E-03	1.03	6.76E-03	1.03
640	3.91E-03	1.02	3.33E-03	1.02

Table 30: Finite Differences WENO5+SSP-RK1 spatial convergence table (converging to $\mathcal{O}(\Delta t)$) approximating the variable coefficient equation $u_t + \left(\frac{u}{1+t}\right)_x = 0$ with initial condition $u_0(x) = e^{-5(x-\pi)^2}$, timestep size $\Delta t = 0.3(\Delta x)$, at final time $T_f = 0.5$.

N_x	L^1 Error	L^1 Order	L^2 Error	L^2 Order
40	1.10E-02	-	9.37E-03	-
80	1.05E-03	3.39	1.06E-03	3.15
160	2.49E-04	2.07	2.15E-04	2.30
320	6.25E-05	2.00	5.41E-05	1.99
640	1.56E-05	2.00	1.35E-05	2.00

Table 31: Finite Differences WENO5+SSP-RK2 spatial convergence table (converging to $\mathcal{O}(\Delta t^2)$) approximating the variable coefficient equation $u_t + \left(\frac{u}{1+t}\right)_x = 0$ with initial condition $u_0(x) = e^{-5(x-\pi)^2}$, timestep size $\Delta t = 0.3(\Delta x)$, at final time $T_f = 0.5$.

N_x	L^1 Error	L^1 Order	L^2 Error	L^2 Order
40	1.16E-02	-	1.02E-02	-
80	8.52E-04	3.76	8.05E-04	3.67
160	3.52E-05	4.60	3.29E-05	4.61
320	1.38E-06	4.67	1.31E-06	4.65
640	7.92E-08	4.12	7.58E-08	4.11

Table 32: Finite Differences WENO5+SSP-RK3 spatial convergence table (exceeding $\mathcal{O}(\Delta t^3)$) approximating the variable coefficient equation $u_t + \left(\frac{u}{1+t}\right)_x = 0$ with initial condition $u_0(x) = e^{-5(x-\pi)^2}$, timestep size $\Delta t = 0.3(\Delta x)$, at final time $T_f = 0.5$.

5 Week 6: 2D WENO5 Finite Difference Solver

5.1 Strang Splitting

Now we extend the WENO5+SSP-RK1/2/3 algorithm to two dimensions. We create a mesh in 2D and use Strang Splitting to update the nodes in x while fixing the y -coordinates and vice-versa. The update method for a single timestep is outlined below:

- 1) Fix y and update for all x using $\frac{\Delta t}{2} \quad u_{ij}^n \rightarrow u_{ij}^*$
- 2) Fix x and update for all y using $\Delta t \quad u_{ij}^* \rightarrow u_{ij}^{**}$
- 3) Fix y and update for all x using $\frac{\Delta t}{2} \quad u_{ij}^{**} \rightarrow u_{ij}^{n+1}$

This is beneficial because it allows us to use the 1D Finite Difference Solver we previously developed to iteratively solve a 2D PDE. However, it also incurs an error of $\mathcal{O}(\Delta t^2)$, which becomes the maximum accuracy the algorithm can achieve. As the spatial accuracy tables show, even when using the third-order accurate WENO5+SSP-RK3 method, we still only achieve second-order accuracy because of the splitting error.

Finally, the CFL condition we previously saw in one dimension can now be translated to two dimensions, yielding

$$CFL = \frac{1}{\frac{\max |f'(u)|}{\Delta x} + \frac{\max |g'(u)|}{\Delta y}}$$

where

$$\frac{\Delta t}{\Delta x} \leq CFL$$

Here we set the CFL condition to be

$$\Delta t \leq 0.95(CFL)$$

5.1.1 Test Case 1: Linear Advection Transport Equation

We first test the 2D Strang-Splitting algorithm on the linear advection transport equation

$$\begin{aligned} u_t + (au)_x + (bu)_y &= 0, \quad (x, y) \in [0, 2\pi] \times [0, 2\pi] \\ u_0(x, y) &= \sin(x + y) \\ T_f &= 0.5 \end{aligned}$$

where a and b are the linear advection speeds in the x and y directions, respectively; for this test, we set $a = 1$ and $b = 2$.

The spatial convergence is shown below in Tables 33, 34, 35.

N_x	L^1 Error	L^1 Order	L^2 Error	L^2 Order
20	2.92E+00	0.00	5.15E-01	0.00
40	1.43E+00	1.03	2.54E-01	1.02
80	7.09E-01	1.02	1.25E-01	1.02
160	3.53E-01	1.01	6.23E-02	1.01
320	1.76E-01	1.00	3.22E-02	0.95

Table 33: 2D Finite Differences WENO5+SSP-RK1 spatial convergence table (converging to $\mathcal{O}(\Delta t)$) approximating the aforementioned linear advection equation with initial condition $u_0(x, y) = \sin(x + y)$, timestep size $\Delta t = 0.95 (CFL)$, at final time $T_f = 0.5$.

N_x	L^1 Error	L^1 Order	L^2 Error	L^2 Order
20	1.72E-01	0.00	2.96E-02	0.00
40	4.25E-02	2.01	7.51E-03	1.98
80	1.06E-02	2.00	1.88E-03	2.00
160	2.66E-03	2.00	4.70E-04	2.00
320	6.65E-04	2.00	1.18E-04	2.00

Table 34: 2D Finite Differences WENO5+SSP-RK2 spatial convergence table (converging to $\mathcal{O}(\Delta t^2)$) approximating the aforementioned linear advection equation with initial condition $u_0(x, y) = \sin(x + y)$, timestep size $\Delta t = 0.95 (CFL)$, at final time $T_f = 0.5$.

N_x	L^1 Error	L^1 Order	L^2 Error	L^2 Order
20	2.13E-02	0.00	3.92E-03	0.00
40	1.45E-03	3.87	2.56E-04	3.94
80	1.42E-04	3.35	2.51E-05	3.35
160	1.66E-05	3.10	2.93E-06	3.10
320	2.03E-06	3.03	3.59E-07	3.03

Table 35: 2D Finite Differences WENO5+SSP-RK3 spatial convergence table (converging to $\mathcal{O}(\Delta t^3)$) approximating the aforementioned linear advection equation with initial condition $u_0(x, y) = \sin(x + y)$, timestep size $\Delta t = 0.95 (CFL)$, at final time $T_f = 0.5$.

The solution surface for the linear advection equation at time $T_f = 0.5$ is shown below in Figure 17

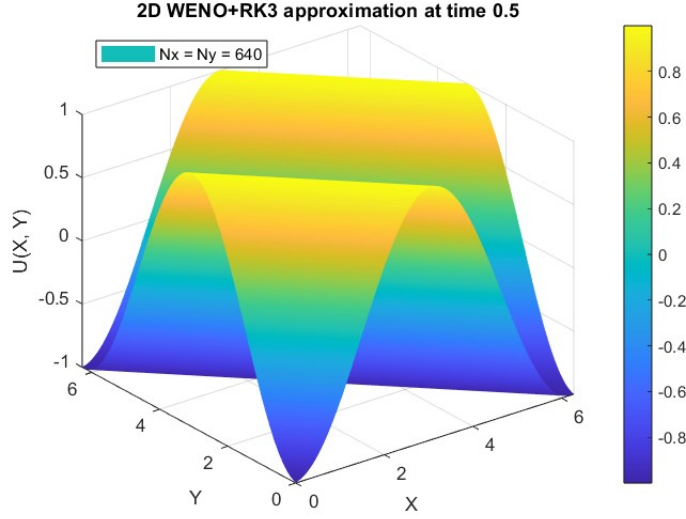


Figure 17: Solution surface approximation using 2D WENO5+SSP-RK3 with spatial mesh size $N_x = N_y = 640$ approximating the linear advection equation with initial condition $u_0(x, y) = \sin(x + y)$ at time $t = 0.5$.

5.1.2 Test Case 2: Rigidbody Rotation

We now test 2D WENO5+SSP-RK1/2/3 on the rigidbody rotation equation with a 2D Gaussian initial condition

$$u_t - (yu)_x + (xu)_y = 0, \quad (x, y) \in [-\pi, \pi] \times [-\pi, \pi]$$

$$u_0(x, y) = e^{-3(x^2+y^2)}$$

$$T_f = 0.5$$

This equation simply rotates the transported quantity around the z-axis. The spatial error convergence is depicted below in Tables 36, 37, 38. Similarly to the linear advection test case, the algorithm loses first-order convergence after high mesh refinement, due to the instability of WENO5+RK1.

N_x	L^1 Error	L^1 Order	L^2 Error	L^2 Order
20	1.74E-01	0.00	1.05E-01	0.00
40	1.80E-02	3.27	1.14E-02	3.20
80	3.67E-03	2.30	1.81E-03	2.66
160	1.77E-03	1.05	8.59E-04	1.07
320	8.91E-04	0.99	4.29E-04	1.00

Table 36: 2D Finite Differences WENO5+SSP-RK1 spatial convergence table (converging to $\mathcal{O}(\Delta t)$) approximating the aforementioned rigidbody rotation equation with initial condition $u_0(x, y) = e^{-3(x^2+y^2)}$, timestep size $\Delta t = 0.95(CFL)$, at final time $T_f = 0.5$.

N_x	L^1 Error	L^1 Order	L^2 Error	L^2 Order
20	1.78E-01	0.00	1.06E-01	0.00
40	1.75E-02	3.35	1.16E-02	3.19
80	1.08E-03	4.02	7.50E-04	3.95
160	4.08E-05	4.72	2.80E-05	4.74
320	2.59E-06	3.98	1.43E-06	4.30

Table 37: 2D Finite Differences WENO5+SSP-RK2 spatial convergence table (exceeding $\mathcal{O}(\Delta t^2)$) approximating the aforementioned rigidbody rotation equation with initial condition $u_0(x, y) = e^{-3(x^2+y^2)}$, timestep size $\Delta t = 0.95(CFL)$, at final time $T_f = 0.5$.

N_x	L^1 Error	L^1 Order	L^2 Error	L^2 Order
20	1.78E-01	0.00	1.06E-01	0.00
40	1.75E-02	3.35	1.16E-02	3.19
80	1.08E-03	4.02	7.50E-04	3.95
160	3.96E-05	4.76	2.77E-05	4.76
320	1.44E-06	4.78	9.73E-07	4.83

Table 38: 2D Finite Differences WENO5+SSP-RK3 spatial convergence table (exceeding $\mathcal{O}(\Delta t^3)$) approximating the aforementioned rigidbody rotation equation with initial condition $u_0(x, y) = e^{-3(x^2+y^2)}$, timestep size $\Delta t = 0.95(CFL)$, at final time $T_f = 0.5$.

The solution surface for the rigidbody rotation PDE at time $T_f = 0.5$ is shown below in Figure 18

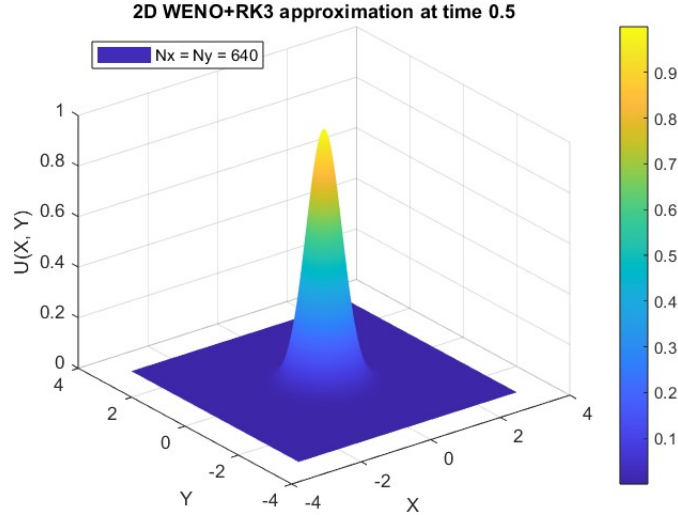


Figure 18: Solution surface approximation using 2D WENO5+SSP-RK3 with spatial mesh size $N_x = N_y = 640$ approximating the rigidbody rotation equation with initial condition $u_0(x, y) = e^{-3(x^2+y^2)}$ at time $t = 0.5$.

5.1.3 Test Case 3: WENO5 Test on 2D Heaviside Step Function

We finally test the 2D Finite Difference WENO5+SSP-RK3 algorithm on the discontinuous two-dimensional Heaviside step function to ensure stable handling of discontinuities. We approximate the following rigidbody rotation PDE at time $T_f = 2\pi$

$$\begin{aligned} u_t - (yu)_x + (xu)_y &= 0, \quad (x, y) \in [-\pi, \pi, -\pi, \pi] \\ u_0(x, y) &= \begin{cases} 1, & (x, y) \in [-1, 1] \times [-1, 1] \\ 0, & \text{otherwise} \end{cases} \\ T_f &= 2\pi \end{aligned} \tag{8}$$

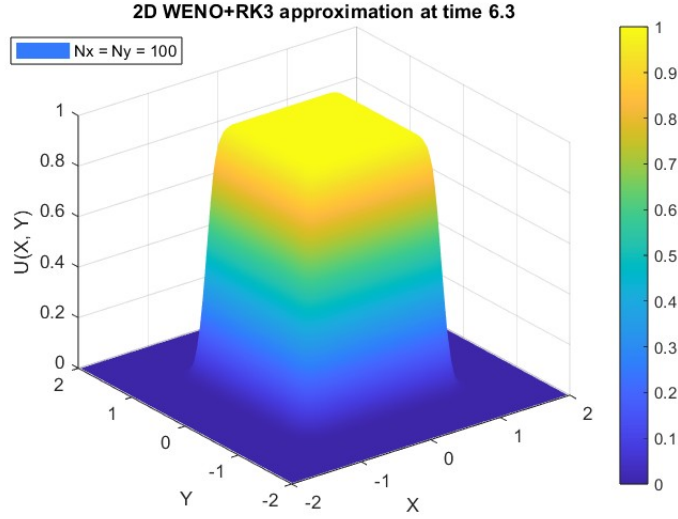


Figure 19: Solution surface approximation using 2D WENO5+SSP-RK3 with spatial mesh size $N_x = N_y = 100$ approximating the linear advection equation with initial condition $u_0(x, y) = e^{(-3(x^2+y^2))}$ at time $t = 0.5$.

We can see that the algorithm elegantly handles the discontinuity without incurring spurious oscillations.

5.2 Test Case 4: Swirling Deformation

We finish by testing the algorithm on the swirling deformation equation

$$u_t - (\cos^2(x/2) \sin(y)g(t)u)_x + (\sin(x) \cos^2(y/2)g(t)u)_y = 0, \quad x, y \in [-\pi, \pi]$$

where

$$g(t) = \cos(t\pi/T_f)\pi$$

and

$$u_0(x, y) = \begin{cases} r_0^b \cos^6\left(\frac{r^b(x, y)\pi}{2r_0^b}\right), & r^b(x, y) < r_0^b \\ 0, & \text{otherwise} \end{cases} \tag{9}$$

where

$$\begin{aligned}
r^b(x, y) &= \sqrt{(x - x_0^b)^2 + (y - y_0^b)^2} \\
r_0^b &= 0.3\pi \\
(x_0^b, y_0^b) &= (0.3\pi, 0) \\
T_f &= 1.5
\end{aligned}$$

The spatial convergence for this swirling deformation problem is shown below in Tables 39, 40, and 41.

N_x	L^1 Error	L^1 Order	L^2 Error	L^2 Order
20	7.55E-02	0.00	5.52E-02	0.00
40	3.81E-02	0.99	3.14E-02	0.82
80	2.26E-02	0.75	2.44E-02	0.36
160	3.33E-02	-0.56	3.81E-02	-0.64
320	1.56E-02	1.10	2.15E-02	0.83

Table 39: 2D Finite Differences WENO5+SSP-RK1 spatial convergence table (converging to $\mathcal{O}(\Delta t)$) approximating the swirling deformation equation at final time $T_f = 1.5$.

N_x	L^1 Error	L^1 Order	L^2 Error	L^2 Order
20	8.92E-02	0.00	6.29E-02	0.00
40	4.42E-02	1.01	3.34E-02	0.91
80	1.92E-02	1.20	2.00E-02	0.74
160	2.70E-03	2.84	5.38E-03	1.90
320	2.45E-04	3.46	1.11E-03	2.27

Table 40: 2D Finite Differences WENO5+SSP-RK2 spatial convergence table (converging to $\mathcal{O}(\Delta t^2)$) approximating the swirling deformation equation at final time $T_f = 1.5$.

N_x	L^1 Error	L^1 Order	L^2 Error	L^2 Order
20	8.89E-02	0.00	6.28E-02	0.00
40	4.43E-02	1.01	3.34E-02	0.91
80	1.92E-02	1.21	2.00E-02	0.75
160	2.71E-03	2.82	5.45E-03	1.87
320	2.51E-04	3.43	1.14E-03	2.26

Table 41: 2D Finite Differences WENO5+SSP-RK3 spatial convergence table (converging to $\mathcal{O}(\Delta t^3)$) approximating the swirling deformation equation at final time $T_f = 1.5$.

We can now test WENO5 on a 2D, discontinuous version of the swirling deformation problem:

$$\begin{aligned}
g(t) &= 1 \\
u_0(x, y) &= \begin{cases} 1 & r^b(x, y) < r_0^b \\ 0, & \text{otherwise} \end{cases}
\end{aligned} \tag{10}$$

$$r_0^b = 8\pi/5$$

$$T_f = 5\pi$$

The numerical solution for the swirling deformation PDE with initial condition 10 is shown below in Figure 20.

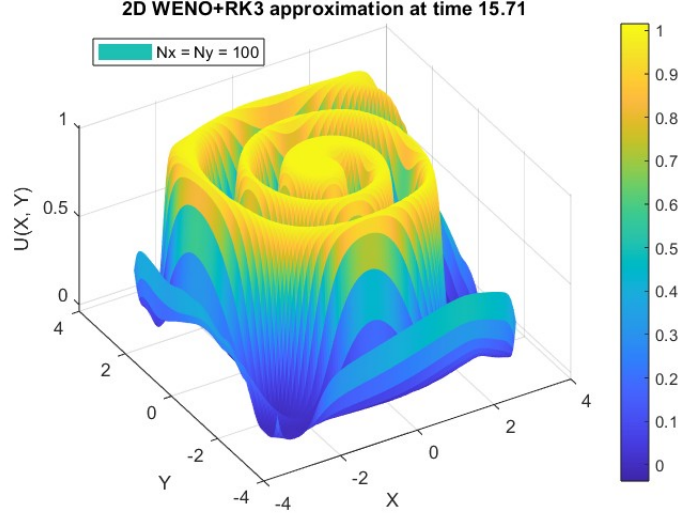


Figure 20: Solution surface approximation using 2D WENO5+SSP-RK3 with spatial mesh size $N_x = N_y = 100$ approximating the swirling deformation equation with initial condition 10 at time $t = 5\pi$.

The algorithm elegantly handles discontinuities, eliminating spurious oscillations.

5.3 Non-Splitting 2D Finite Difference Solver

To eliminate the $\mathcal{O}(\Delta t^2)$ splitting error, we can update our numerical solution in both dimensions simultaneously instead of using Strang Splitting.

We repeat three tests (Linear Advection, Rigidbody Rotation, and Swirling Deformation), keeping constant the CFL condition

$$\frac{\Delta t}{\Delta x} = \frac{0.95}{\frac{\max |f'(u)|}{\Delta x} + \frac{\max |g'(u)|}{\Delta y}}$$

However, this time we test for $\mathcal{O}(\Delta t^3)$ and $\mathcal{O}(\Delta t^4)$ spatial accuracy because we have eliminated the $\mathcal{O}(\Delta t^2)$ Strang Splitting error.

5.3.1 Test Case 1: Linear Advection

N_x	L^1 Error	L^1 Order	L^2 Error	L^2 Order
20	5.42E-02	-	9.41E-03	-
40	5.60E-03	3.28	9.88E-04	3.25
80	6.62E-04	3.08	1.17E-04	3.08
160	8.16E-05	3.02	1.44E-05	3.02
320	1.02E-05	3.01	1.80E-06	3.00

Table 42: 2D Non-Splitting Finite Differences WENO5+SSP-RK3 spatial convergence table (converging to $\mathcal{O}(\Delta t^3)$) approximating the aforementioned linear advection equation with initial condition $u_0(x, y) = \sin(x + y)$, timestep size $\Delta t = 0.95$ (CFL), at final time $T_f = 0.5$.

N_x	L^1 Error	L^1 Order	L^2 Error	L^2 Order
20	1.58E-02	-	2.89E-03	-
40	4.81E-04	5.04	9.00E-05	5.00
80	1.70E-05	4.83	3.10E-06	4.86
160	7.45E-07	4.51	1.33E-07	4.54
320	4.02E-08	4.21	7.12E-09	4.22

Table 43: 2D Non-Splitting Finite Differences WENO5+RK4 spatial convergence table (converging to $\mathcal{O}(\Delta t^4)$) approximating the aforementioned linear advection equation with initial condition $u_0(x, y) = \sin(x + y)$, timestep size $\Delta t = 0.95$ (CFL), at final time $T_f = 0.5$.

The solution surface for the linear advection equation at time $T_f = 0.5$ is shown below in Figure 21

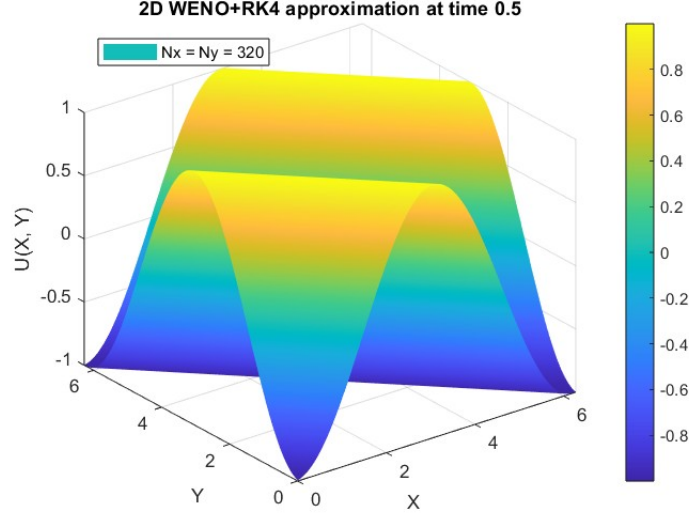


Figure 21: Solution surface approximation using 2D WENO5+RK4 with spatial mesh size $N_x = N_y = 320$ approximating the linear advection equation with initial condition $u_0(x, y) = \sin(x + y)$ at time $t = 0.5$.

5.3.2 Test Case 2: Rigidbody Rotation

N_x	L^1 Error	L^1 Order	L^2 Error	L^2 Order
20	1.78E-01	-	1.06E-01	-
40	1.75E-02	3.35	1.16E-02	3.19
80	1.08E-03	4.02	7.50E-04	3.95
160	3.95E-05	4.77	2.77E-05	4.76
320	1.27E-06	4.96	8.95E-07	4.95

Table 44: 2D Non-Splitting Finite Differences WENO5+SSP-RK3 spatial convergence table (exceeding $\mathcal{O}(\Delta t^3)$) approximating the rigidbody rotation equation with initial condition $u_0(x, y) = e^{(-3(x^2+y^2))}$, timestep size $\Delta t = 0.95(CFL)$, at final time $T_f = 0.5$.

N_x	L^1 Error	L^1 Order	L^2 Error	L^2 Order
20	1.78E-01	-	1.06E-01	-
40	1.75E-02	3.35	1.16E-02	3.19
80	1.08E-03	4.02	7.50E-04	3.95
160	3.95E-05	4.77	2.77E-05	4.76
320	1.27E-06	4.96	8.95E-07	4.95

Table 45: 2D Non-Splitting Finite Differences WENO5+RK4 spatial convergence table (exceeding $\mathcal{O}(\Delta t^4)$) approximating the rigidbody rotation equation with initial condition $u_0(x, y) = e^{(-3(x^2+y^2))}$, timestep size $\Delta t = 0.95(CFL)$, at final time $T_f = 0.5$.

The numerical solution for the rigidbody rotation PDE at time $T_f = 0.5$ is shown below in Figure 22

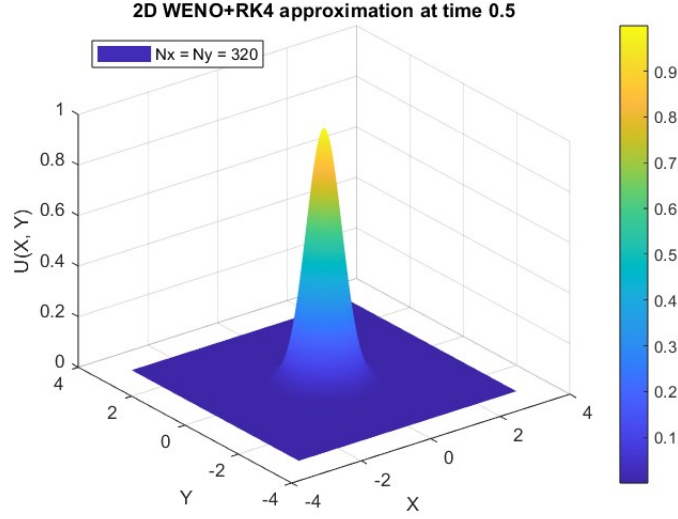


Figure 22: Numerical solution using 2D WENO5+RK4 with spatial mesh size $N_x = N_y = 320$ approximating the rigidbody rotation PDE with initial condition $u_0(x, y) = e^{-3(x^2+y^2)}$ at time $t = 0.5$.

5.3.3 Test Case 3: Swirling Diffusion

We finally test the non-splitting algorithm on the swirling deformation equation

$$u_t - (\cos^2(x/2) \sin(y) g(t) u)_x + (\sin(x) \cos^2(y/2) g(t) u)_y = 0, \quad x, y \in [-\pi, \pi]$$

where

$$g(t) = \cos(t\pi/T_f)\pi$$

and

$$u_0(x, y) = \begin{cases} r_0^b \cos^6\left(\frac{r^b(x, y)\pi}{2r_0^b}\right), & r^b(x, y) < r_0^b \\ 0, & \text{otherwise} \end{cases} \quad (11)$$

where

$$r^b(x, y) = \sqrt{(x - x_0^b)^2 + (y - y_0^b)^2}$$

$$r_0^b = 0.3\pi$$

$$(x_0^b, y_0^b) = (0.3\pi, 0)$$

$$T_f = 1.5$$

The spatial convergence for this swirling deformation problem is shown below in Tables 46 and 47.

N_x	L^1 Error	L^1 Order	L^2 Error	L^2 Order
20	8.89E-02	-	6.28E-02	-
40	4.42E-02	1.01	3.34E-02	0.91
80	1.92E-02	1.21	2.00E-02	0.74
160	2.71E-03	2.82	5.46E-03	1.87
320	2.50E-04	3.44	1.14E-03	2.26

Table 46: 2D Non-Splitting Finite Differences WENO5+SSP-RK3 spatial convergence table (converging to $\mathcal{O}(\Delta t^3)$) approximating the swirling deformation equation at final time $T_f = 1.5$.

N_x	L^1 Error	L^1 Order	L^2 Error	L^2 Order
20	8.88E-02	-	6.27E-02	-
40	4.42E-02	1.01	3.34E-02	0.91
80	1.92E-02	1.21	1.99E-02	0.74
160	2.70E-03	2.82	5.43E-03	1.88
320	2.49E-04	3.44	1.13E-03	2.26

Table 47: 2D Non-Splitting Finite Differences WENO5+RK4 spatial convergence table (approaching $\mathcal{O}(\Delta t^4)$) approximating the swirling deformation equation at final time $T_f = 1.5$.

The numerical solution for the swirling deformation PDE at time $T_f = 1.5$ is shown below in Figure 23

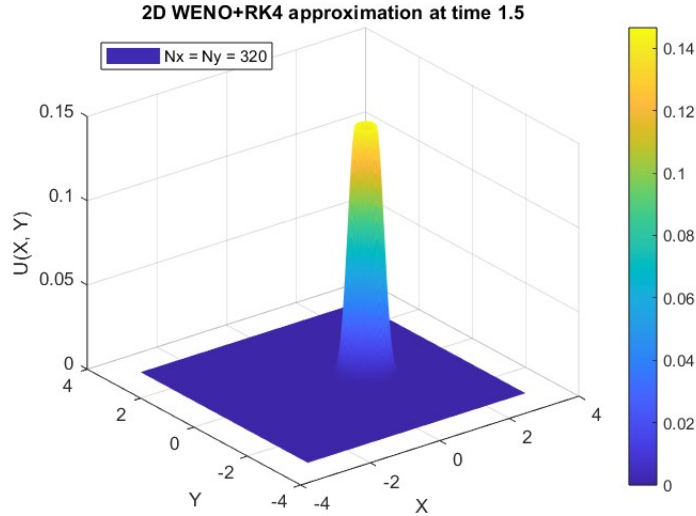


Figure 23: Numerical solution using 2D WENO5+RK4 with spatial mesh size $N_x = N_y = 320$ approximating the swirling deformation PDE at time $t = 1.5$.

We can now ensure that WENO5 works correctly by testing the algorithm on a 2D, discontinuous version of the swirling deformation problem:

$$g(t) = 1$$

$$u_0(x, y) = \begin{cases} 1 & r^b(x, y) < r_0^b \\ 0, & \text{otherwise} \end{cases} \quad (12)$$

$$r_0^b = 8\pi/5$$

$$T_f = 5\pi$$

The numerical solution for the swirling deformation PDE with initial condition 12 is shown below in Figure 24.

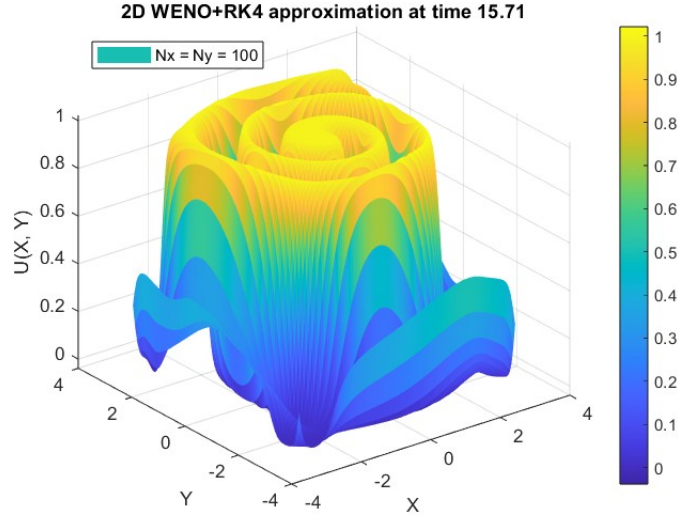


Figure 24: Numerical solution using 2D WENO5+RK4 with spatial mesh size $N_x = N_y = 100$ approximating the swirling deformation equation with initial condition (12) at time $t = 5\pi$.

The algorithm elegantly handles discontinuities, eliminating spurious oscillations.

6 Week 7: Vlasov-Poisson Solver

We now slightly modify and apply our Two-Dimensional First-Order PDE solver to the Vlasov-Poisson Equation.

$$f_t + (vf)_x + (E(x,t)f)_v = 0$$

where v represents velocity, x represents one spatial dimension, $E(x,t)$ defines energy with respect to x and t , and $f(x,v,t)$ is the distribution of particles in the system. We can use the two-dimensional PDE solver we previously built to solve this system by updating $\beta = \max |E(x,t)|$ every time-step because E depends on time. We first compute the energy density ρ by summing f across the v dimension. This can then be used to compute E using Poisson's Equation:

$$E = -\nabla_x \phi$$

$$\phi_{xx} = -\rho(x,t) = -\left(\int_{\mathbb{R}} f(x,v,t)dV - 1\right)$$

We sum across f to find ρ , which we then scale by subtracting one. Using algebraic manipulation, and Fourier/Inverse Fourier Transformations, we find that

$$E = \mathcal{F}^{-1}\left\{\frac{-i}{k}\mathcal{F}\{\rho\}\right\}$$

Finally, we update β based on E and proceed with the Runge-Kutta time-step. We test a nonsplitting, finite-difference WENO5+SSP-RK3 algorithm on three different test cases: Weak-Landau Damping, Strong-Landau Damping, and Two-Stream Instability.

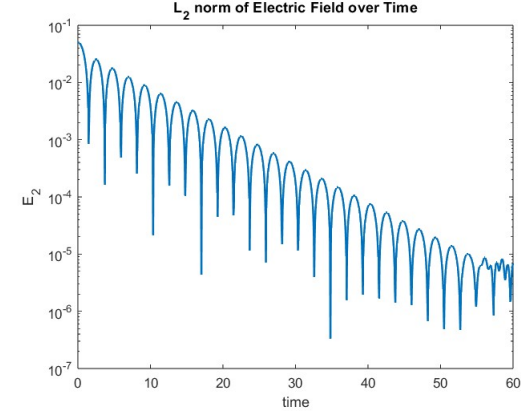
6.1 Test Case 1: Weak Landau Damping

We first test the algorithm on the Vlasov-Poisson Equation with the following initial conditions:

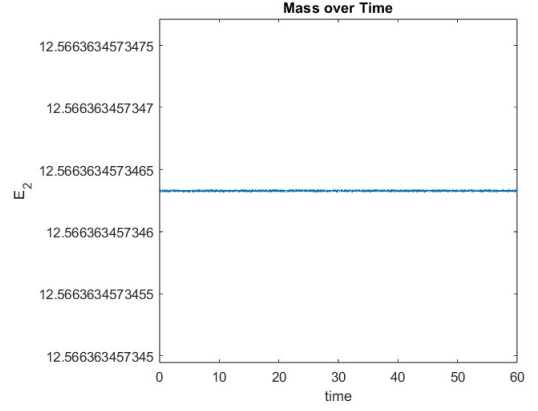
$$f_0 = \frac{1}{\sqrt{2\pi}} \left(1 + \alpha \cos(kx)e^{-0.5v^2}\right)$$

$$\alpha = 0.01, \quad k = 0.5$$

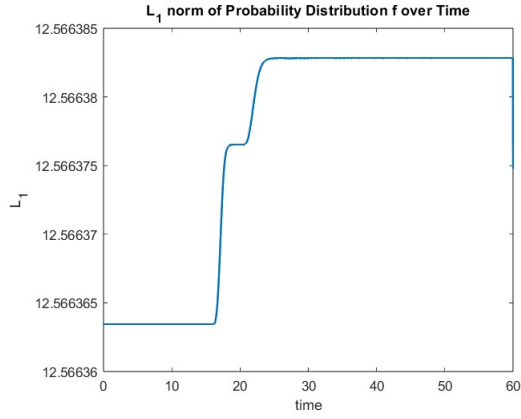
We discretize using mesh size $N_x = 64, N_v = 128$ on the interval $x \in [0, 4\pi], v \in [-5, 5]$ with time-step $\Delta t = 0.3\Delta x$ and run the simulation until time $t = 60$. We can plot the physical components of our system to ensure it obeys conservation laws (e.g. conservation of energy and mass). As shown in Figure 25, the physical constants are relatively stable over time, varying only slightly. Interestingly, entropy decreases slightly during the first half of the time period, increasing again after time $t \approx 23$.



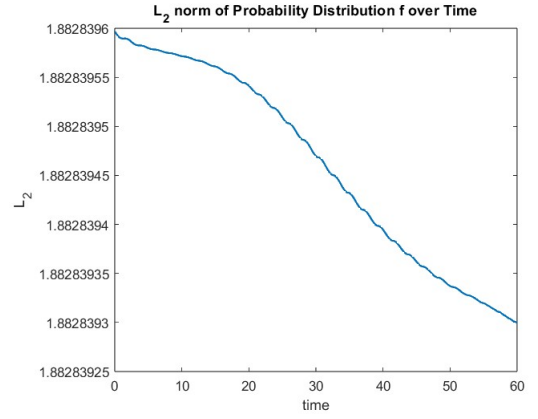
(a)



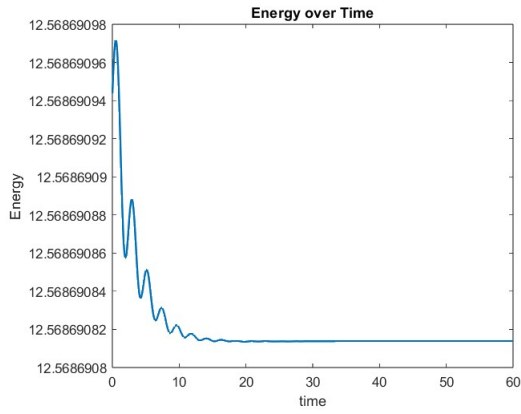
(b)



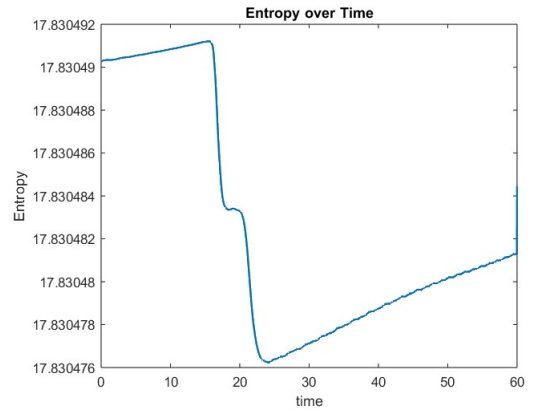
(c)



(d)



(e)



(f)

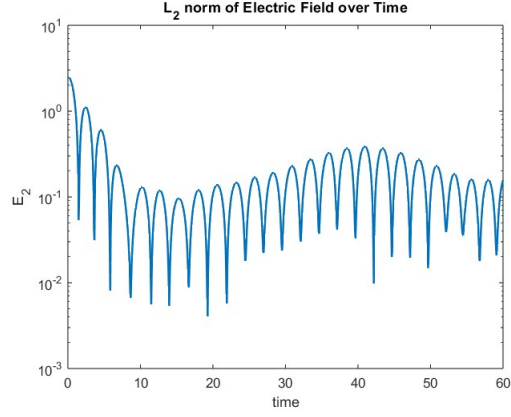
Figure 25: Graphs demonstrating conservative properties of the Vlasov-Poisson solver for the Weak-Landau Damping Test Case. a) L^2 norm of the electrical field $E(x, t)$ over time. b) mass plot over time. c) L^1 norm of the numerical solution over time. d) L^2 norm of the numerical solution over time. e) Energy over time (Riemann sum). f) Entropy over time (Riemann sum)

6.2 Test Case 2: Strong Landau Damping

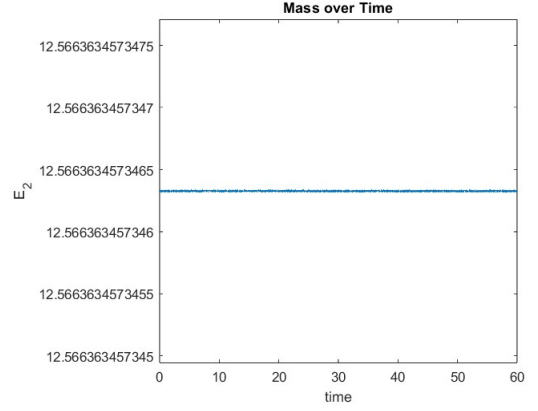
We now test the algorithm on the Vlasov-Poisson Equation with strong Landau damping ($\alpha = 0.5$):

$$f_0 = \frac{1}{\sqrt{2\pi}} \left(1 + \alpha \cos(kx) e^{-0.5v^2} \right)$$
$$\alpha = 0.5, \quad k = 0.5$$

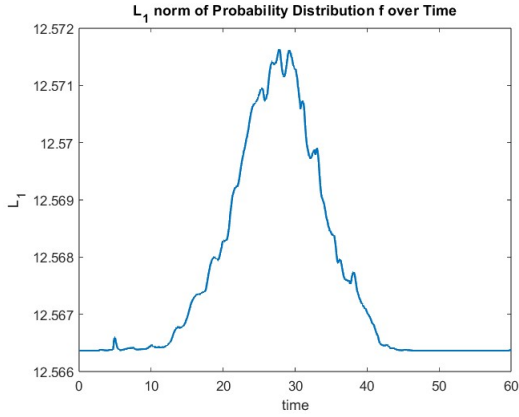
Using the same mesh size, CFL condition, and time period yields the plots shown in Figure 26. As depicted, the L^1 , and L^2 norms of the solution vary only slightly, energy and entropy increase marginally more, and the electric field oscillates and varies over time.



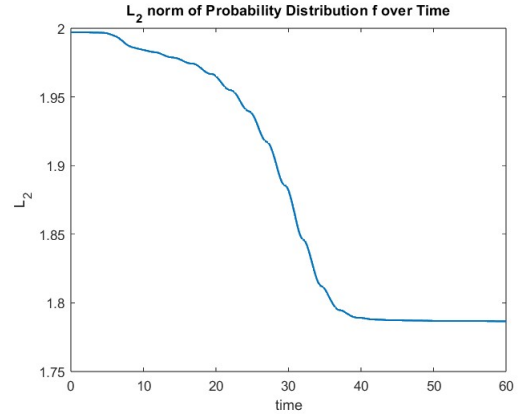
(a)



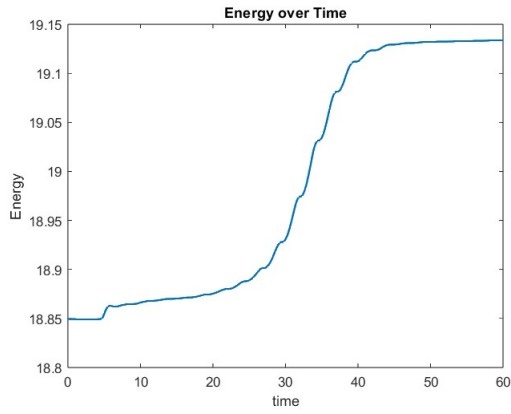
(b)



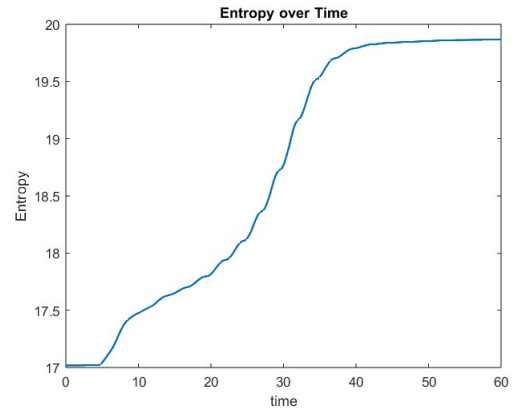
(c)



(d)



(e)



(f)

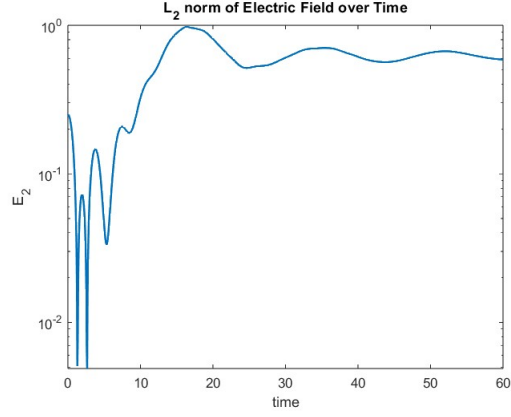
Figure 26: Graphs demonstrating conservative properties of the Vlasov-Poisson solver for the Strong-Landau-Damping Test Case. a) L^2 norm of the electrical field $E(x, t)$ over time. b) mass plot over time. c) L^1 norm of the numerical solution over time. d) L^2 norm of the numerical solution over time. e) Energy over time (Riemann sum). f) Entropy over time (Riemann sum)

6.3 Test Case 3: Two-Stream Instability

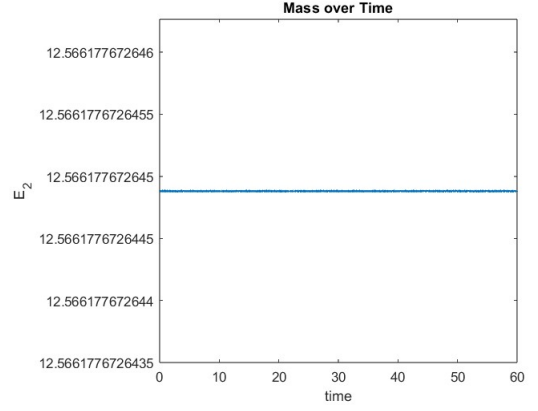
We finish testing the solver on the following test case:

$$f_0 = \frac{1}{\sqrt{2\pi}} \left(1 + \alpha \cos(kx) e^{-0.5v^2} \right) v^2$$
$$\alpha = 0.05, \quad k = 0.5$$

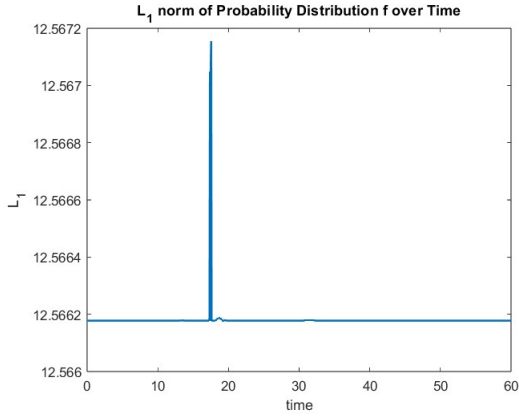
The conservation plots are shown in Figure 27 and the numerical solution at time $t = 60$ is shown in Figure 28.



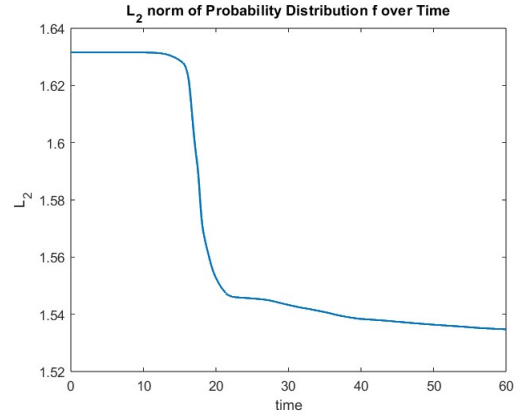
(a)



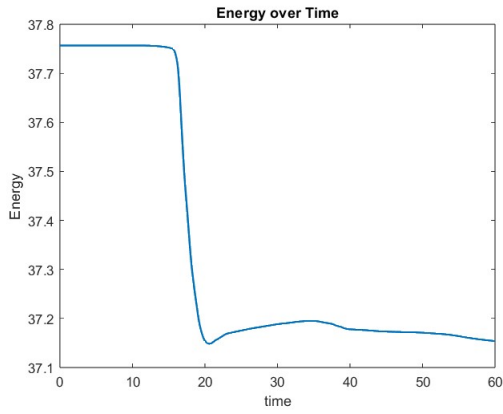
(b)



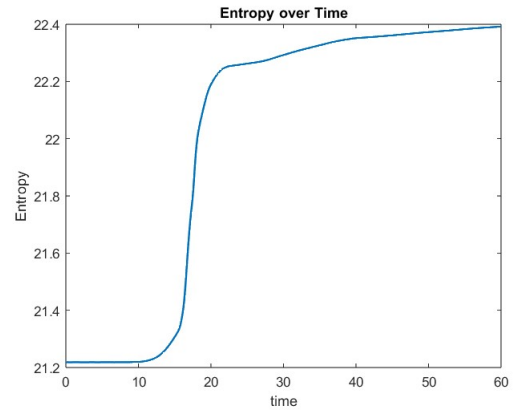
(c)



(d)



(e)



(f)

Figure 27: Graphs demonstrating conservative properties of the Vlasov-Poisson solver for the Two-Stream Instability Test Case. a) L^2 norm of the electrical field $E(x, t)$ over time. b) mass plot over time. c) L^1 norm of the numerical solution over time. d) L^2 norm of the numerical solution over time. e) Energy over time (Riemann sum). f) Entropy over time (Riemann sum)

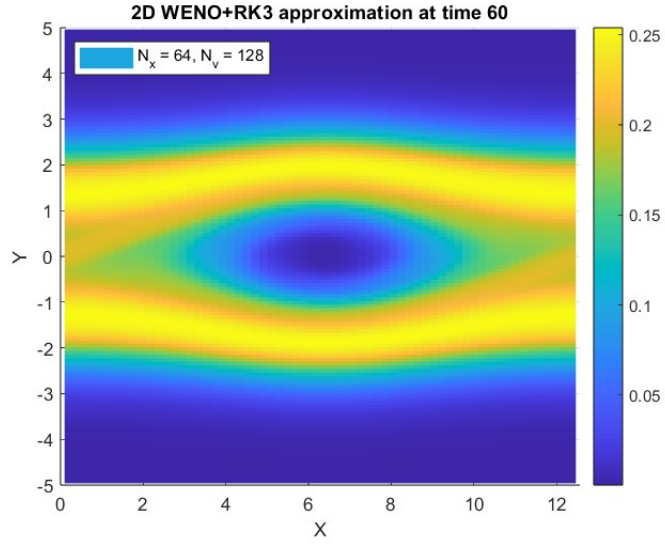


Figure 28: Numerical solution of the Two-Stream Instability problem at time $t = 60$ using mesh size $N_x = 64$ and $N_y = 128$ with CFL condition $\Delta t = 0.3\Delta x$.

6.4 Flop Tests

In this section, we briefly depart from numerical PDE approximation to analyze the computational cost of various data-compression methods, including Single Variable Decomposition (SVD) and QR Factorization. For SVD with matrix $A \in \mathbb{C}^{m \times n}$, the number of flops—floating-point operations—should approach $\mathcal{O}(2mn^2)$ because for each cell in the $m \times n$ sized matrix A , there are $2n$ operations (n additions + n multiplications). Similarly, for full QR factorization, there should be $\sim \mathcal{O}(2m^3)$ operations because the algorithm maintains the square condition $m = n$ for row number m and column number n . However, the "economy" or reduced QR factorization algorithm should approach $\mathcal{O}(2mn^2)$, which is apparent in column 3 of Table 48, which shows the results of QR factorization on a random "skinny" matrix of size $m \times \frac{m}{10}$, $\forall m \in [40, 80, 160, 320, 640, 1280, 2560]$. In addition to testing SVD and QR factorization, we verify that the order of matrix multiplication matters for flop counts. In the first matrix multiplication test, we determine the runtime for the operation $(AB)C$ where $A, B \in \mathbb{C}^{m \times m}$ and $C \in \mathbb{C}^{m \times \frac{m}{10}}$. We compare that against the second matrix multiplication operation $A(BC)$, finding that the second is significantly faster, both in runtime and order.

M	SVD		QR Factorization		Skinny Qr Factorization		Matrix Multiplication 1		Matrix Multiplication 2	
	Runtime	Order	Runtime	Order	Runtime	Order	Runtime	Order	Runtime	Order
40	0.0006415	-	0.0001399	-	4.04E-05	-	6.90E-05	-	0.0001562	-
80	0.0011326	0.82012	0.0003182	1.1855	5.81E-05	0.52418	8.54E-05	0.30764	4.32E-05	-1.8543
160	0.0035956	1.6666	0.0010784	1.7609	0.0001437	1.3064	0.0002139	1.3246	9.32E-05	1.1093
320	0.014521	2.0138	0.0023028	1.0945	0.0002852	0.98891	0.0009852	2.2035	0.0002763	1.5678
640	0.062584	2.1077	0.0096495	2.0671	0.0011214	1.9753	0.0053532	2.4419	0.0014382	2.38
1280	0.44954	2.8446	0.074208	2.943	0.0083876	2.903	0.045233	3.0789	0.012296	3.0959
2560	4.2589	3.244	0.49001	2.7232	0.029909	1.8343	0.23808	2.396	0.056554	2.2015

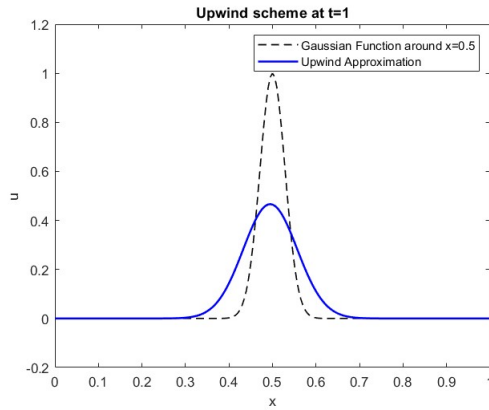
Table 48: Flop Tests for SVD, QR Factorization, Skinny QR Factorization, and Matrix Multiplication

7 Appendix

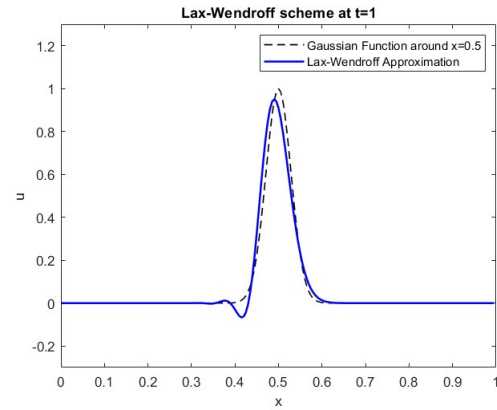
7.1 Week 2

7.2 Approximated solution curves for linear advection equation with an initial condition of the Gaussian Exponential Function around $x = 0.5$

$$u(x, t = 0) = \exp(-600(x - 0.5)^2)$$



(a) Solution curve for upwind scheme approximating the Gaussian function around $x = 0.5$



(b) Solution curve for Lax-Wendroff Method approximating the Gaussian function around $x = 0.5$

Figure 29: Gaussian Function Approximation Plots